Analysis of Crossflow Transition Flight Experiment aboard the Pegasus Launch Vehicle

Mujeeb R. Malik*
NASA Langley Research Center, Hampton, VA 23681

Fei Li†
National Institute of Aerospace, Hampton, VA 23666

and

Meelan Choudhari‡
NASA Langley Research Center, Hampton, VA 23681

The Pegasus wing-glove flight experiment[1-4] was designed to provide crossflow transition data at high Mach numbers, specifically to help validate stability based predictions for transition onset in a flight environment. This paper provides an analysis of the flight experiment, with emphasis on computational results for crossflow disturbances and the correlation of disturbance growth factors with in-flight transition locations via the e^N method. Implications of the flight data for attachment line stability are also examined. Analysis of the thermocouple data reveals that transition (from turbulent to laminar flow) was first detected during the ascending flight of the rocket when the free stream Mach number exceeded about 4. Therefore, computations have been performed for flight Mach numbers of 4.13, 4.35, 4.56 and 4.99. Due to continually decreasing unit Reynolds number at higher altitudes, the entire wing-glove boundary layer became laminar at the highest flight Mach number computed above. In contrast, the boundary layer flow over the inboard tile region remained transitional up to and somewhat beyond the time of laminarization over the instrumented glove region. Linear stability predictions confirmed that the tile boundary layer is indeed more unstable to crossflow disturbances than the much colder stainless steel glove boundary layer. The transition locations based on thermocouple data from both the glove and the tile regions are found to correlate with stationary-crossflow N-factors within the range of 7 to 12.4 and with traveling mode N-factors between 7.6 and 14.1. Data from the thermocouples and hot film sensors indicates that transition from turbulent to laminar flow (i.e., laminarization) at a fixed point over the glove is generally completed within a flight time interval of 3 seconds. However, the times at which transition begins and ends as inferred from the hot film sensors are found to differ by about 2 seconds from the corresponding estimates based on the thermocouple data.

*Head, Computational Aerosciences Branch, M.S. 128, 15 Langley Boulevard, AIAA Associate Fellow
†Senior Research Scientist, 100 Exploration Way.
‡Senior Research Scientist, Computational Aerosciences Branch, M.S. 128, 13 Langley Boulevard, AIAA Associate Fellow

Nomenclature

A	disturbance amplitude
A_0	disturbance amplitude at neutral point
C_p	pressure coefficient
I, J, K	grid indices
M	Mach number
N	N factor
Pr	Prandtl number
R_{cf}	$\left\|V\right\|_{\max}\delta_1 / \nu_e$; crossflow Reynolds number
$\overline{R}$	$w_e\delta / \nu_e$; attachment-line Reynolds number
Re	unit Reynolds number
R_θ	Reynolds number based on momentum thickness
T	temperature
T_{aw}	$T_e\left(1+\frac{\gamma-1}{2}M_e^2\sqrt{\Pr}\right)$; adiabatic wall temperature
T^*	$T_e + 0.1\left(T_w - T_e\right) + 0.6\left(T_{aw} - T_e\right)$; reference wall temperature
U	streamwise velocity
V	crossflow velocity
X	longitudinal coordinate measured from the wing trailing edge, pointing forward.
Y	spanwise coordinate measured from the fuselage center line
a_∞	freestream speed of sound
c	wing chord length
p	pressure
s	distance along a line on body surface
t	time
u	chordwise velocity perpendicular to attachment line
w	velocity along attachment line
x	longitudinal coordinate measured from the wing leading edge
y	boundary layer vertical coordinate
δ	$\sqrt{\nu_e / \left(du_e / ds\right)}$; characteristics length scale
δ_1	distance from wall where V reduces to $0.1\left\|V\right\|_{\max}$
γ	specific heat ratio
κ_s	$\frac{\nu}{U_e^2}\frac{du_e}{ds}\cos^2\psi_e$; flow acceleration parameter
ν	kinematic viscosity
ρ	air density
σ	disturbance growth rate
ψ_e	angle between inviscid streamline and a line perpendicular to attachment-line

Subscripts:

aw	adiabatic wall
e	boundary layer edge value

w wall
∞ freestream value

Supercript:

$*$ evaluated at reference temperature T^*

I. Introduction

Boundary layer transition is a complex phenomenon and myriads of factors including body geometry, surface finish, temperature, Mach number, flow chemistry and free stream environment (acoustic, vortical and entropy disturbances) determine the Reynolds number at which the flow begins to transition from the laminar to a turbulent state. Depending upon surface roughness and the level of free stream disturbances, transition can occur via different paths as reviewed by Reshotko[5]. Given a smooth surface and very low levels of free stream disturbances, transition occurs through amplification of boundary layer instability modes described within the framework of linear stability theory. In this context, the transition onset Reynolds number can be determined by using the e^N method[6] where the exponent, known as *N* factor, is given as

$$N = \ln(A / A_0) = \int_S \sigma \, ds \qquad (1)$$

Here, σ denotes the spatial growth rate of a boundary layer disturbance as determined by the eigenvalue problem of linear stability theory or by solving the parabolized stability equations which account for the additional effects of boundary layer growth and surface curvature. Integration in Eq. (1) is carried out along a trajectory *s* along the body surface, starting from a location where the boundary layer disturbances first begin to amplify (i.e., at the location of neutral stability). In Eq. (1), the quantity *A* represents the amplitude of boundary layer disturbances and A_0 denotes its value at the neutral point. The value of N is determined via correlation with a relevant set of measured transition locations.

In practice, transition may be expected to occur when the boundary layer disturbances have reached sufficiently large amplitudes, so that the value of *N* should increase as the initial amplitude A_0 becomes smaller. For the low levels of free stream disturbances typical of external aeronautical flows, $N \approx 10$ is found to correlate with transition in a broad class of flows.

Two-dimensional and axisymmetric boundary layers at supersonic and hypersonic Mach numbers can support first and second mode instabilities, which were studied theoretically by Mack[7]. Transition within these flows has been experimentally investigated in both conventional (noisy) and quiet (low disturbance) wind tunnels. Quiet tunnels have low levels of free stream disturbances and tend to simulate in-flight transition, at least in terms of correlating the transition onset with the same value of N factor, as found by Malik[8-9] and Chen et al.[10] for the first and second mode disturbances. Conventional tunnels yield lower values of N factors (Chen et al.[10], Horvath et al. [11]), owing to elevated levels of free-stream disturbances.

There is little information available about transition in supersonic and hypersonic three-dimensional boundary layers in low disturbance environments. The only flight experiment is that of F16-XL-2[12], which was designed for laminar flow control using suction. King[13] performed experiments in NASA Langley's Mach 3.5 quiet tunnel on a sharp cone at incidence and Cattafesta[14-15] performed experiments on a delta wing model in the same facility, both without and with wall suction. Flight transition data for three dimensional boundary layers at higher Mach numbers is lacking.

A. Transition in Three-Dimensional Boundary Layers

There are several instability mechanisms that may cause laminar-turbulent transition in the three-dimensional boundary layer flow over a swept wing. First, attention needs to be given to the attachment-line boundary layer, which can become unstable to Tollmien-Schlichting (TS) or first-mode (Mack [7]) disturbances (Hall et al.[16], Lin and Malik[17-18], Theofilis et al.[19], Coleman et al.[20]). However, the attachment-line boundary layer can sustain turbulence even at sub-critical Reynolds numbers. Based on experimental results at low subsonic Mach numbers (Pfenninger and Bacon[21] and Poll[22], the attachment-line boundary layer can remain laminar in the presence of contamination

from either a turbulent fuselage boundary layer or transition caused by surface roughness/trips only when the Reynolds number parameter $\overline{R} = w_e \delta / \nu_e$ (where W_e is the inviscid slip velocity along the attachment line, $\delta = \sqrt{\nu_e / (du_e / ds)}$ denotes the length scale based on local strain rate, and υ_e is the kinematic viscosity) does not exceed a value of approximately 245 (or, alternatively, $R_\theta < 100$). A similar criterion for avoiding contamination is applicable to supersonic attachment-line boundary layers (Creel et al.[23], Poll[24], Arnal et al.[25], Murakami et al.[26]). Since $\overline{R}$ varies directly with the leading-edge radius, the latter has to be minimized if the goal is to maintain a laminar attachment-line boundary layer. When higher leading-edge Reynolds numbers cannot be avoided, wall suction must be used (Poll and Danks[27]) for swept-wing laminar flow control.

Downstream of the attachment line, the three-dimensional boundary layer becomes subject to crossflow instability (Gregory et al.[28]), which is an inviscid instability of the inflectional velocity profiles in the crossflow direction (i.e., in a direction normal to the inviscid streamlines). The three-dimensional boundary layer can support both stationary and traveling modes of crossflow instability. In practice, the crossflow instability often manifests itself in the form of stationary, co-rotating streamwise vortices, and leads to laminar-turbulent breakdown via a secondary instability mechanism that was studied theoretically by Malik et al.[29-30] and experimentally by Kohama et al.[31] and White and Saric[32]. Depending upon environmental forcing, traveling crossflow disturbances may also be present in three-dimensional boundary layers (Malik et al.[29]), Itoh[33], Mueller and Bippes[34]). The frequency of these disturbances is generally much lower than TS/first-mode waves and their direction of propagation with respect to the inviscid streamlines is more oblique in comparison with the first-mode disturbances.

Crossflow instability can be controlled either by applying wall suction or by designing the wing to have a flat roof-top pressure distribution. However, in the latter case the boundary layer becomes subject to TS instability (for subsonic flow) or first-mode instability (for supersonic flow). For even higher Mach numbers (M > 4) and flat roof-top pressure distribution, Mack's[35] high frequency second mode disturbances may constitute the primary instability mechanism, particularly for cold walls. Transition induced by stationary crossflow disturbances may be controlled by spanwise periodic roughness elements (Saric and Reed[36]), at least for a limited range of Reynolds numbers.

In general, the crossflow or TS type disturbances become relevant to the transition process only if the attachment-line boundary layer remains laminar as, otherwise, the whole wing boundary layer will be turbulent. However, for a range of Reynolds numbers and strong favorable surface pressure gradients, it is possible for a turbulent boundary layer to relaminarize (van Dam et al.[37]), in which case the swept-wing boundary layer can re-transition via one of the mechanisms discussed above.

The Pegasus wing-glove experiment conducted by Bertelrud et al.[1-4] was designed to study crossflow induced laminar-turbulent transition at a flight Mach number of 6. For this purpose, the glove was designed to maximize favorable pressure gradients along the wing surface, in order to enhance crossflow (over first- and second-mode streamwise instabilities) while minimizing the leading-edge radius to maintain a laminar attachment-line boundary layer for the conditions of interest. Static and dynamic instrumentation for in-flight detection of boundary layer transition were provided. A brief description of the experiment, instrumentation and transition data acquired is given below. For additional details of the pre-flight design, instrumentation scheme, and the glove manufacture, the reader is directed to references[1-4].

B. The Pegasus Flight Experiment

The 1998 wing-glove flight experiment of Bertelrud et al.[1-4] was performed aboard the Orbital Sciences Pegasus launch vehicle. The plan view and layout of the Pegasus vehicle are shown in Fig. 1. The stated purpose of the experiment was to achieve and document crossflow-induced boundary-layer transition in the hypersonic regime. A wing glove was designed with the goal to achieve transition at a flight Mach number of 6. The Pegasus rocket, carried under the belly of a Lockheed L1011, cruising at Mach 0.83, was released at an altitude of 38,600 ft. Following ignition at 5 seconds after the release, the rocket accelerated to a Mach number of about 8 as it reached a peak altitude of approximately 240,000 ft. The rocket then descended and dropped into the ocean. Contrary to the expectations based on pre-flight design computations, the glove boundary layer transitioned from turbulent to laminar at a Mach number of between 4 and 4.5 and was found to be completely laminar at the design Mach number of 6. Transition data on the much hotter inboard tile region are available up to about Mach 5.3.

The glove leading edge was machined from a relatively thick steel block, which was joined (see Fig. 2) to a steel sheet of 2.3 mm thickness using screws and the soldering process. The glove surface was smoothed and polished and the maximum peak to valley roughness height of the glove surface was measured to be less than 1 micron. The

glove was installed on starboard side of the 45-degree swept delta wing of the Pegasus vehicle using Balsa wood support and swivel studs (Ref [1-4]). The swivel studs were used to allow the glove skin to move outboard owing to thermal expansion without deformation and buckling. Figure 3 shows a photograph of the actual glove embedded within a ceramic tile boundary. The design allowed the glove skin to slide over the outboard and trailing edge ceramic tiles to accommodate thermal expansion. Figure 4 is a preflight photograph of the assembly and indicative of the mirror finish of the glove surface.

The glove was instrumented with pressure probes and thermocouples to measure surface pressure and temperature, respectively. In addition, dynamic sensors (hot film and pressure transducers) were placed near the trailing edge of the glove in order to characterize the local flow fluctuations. A row of thermocouples was also provided in the inboard tile region. Other instrumentation (pressure rake, Preston tubes, Stanton tubes, etc.) was also provided as described in Refs. [1–4].

The locations of the two rows of pressure probes located near the inboard and outboard edges of the glove are shown in Fig. 5. In addition, the locations of the aft pressure taps and the pressure rake are also shown. The diameter of each pressure port was .0625 inches and the layout was designed to not affect the thermocouple readings even if these ports act as boundary layer trips. There is no evidence to suggest that these ports tripped the boundary layer. The inboard-tile, inboard, center and outboard rows of thermocouples on the glove, as well as the two extra rows of thermocouples and high frequency sensors, are shown in Fig. 6. The thermocouples on the glove are mounted immediately underneath the thin stainless steel skin. The temperature and heat flux on the surface above the skin are computed by solving a one-dimensional inverse heat conduction problem[38].

Figure 7 shows the flight Mach number, altitude and unit Reynolds number as functions of flight time. The position and the velocity of the Pegasus vehicle were measured with a global positioning system and the 1976 Standard Atmosphere was used to compute the Mach number and the Reynolds number. Figure 7 shows that both Mach number and altitude of the vehicle increase monotonically over the time interval plotted in the figure. On the other hand, the unit Reynolds number peaks around 25 seconds into the flight and decreases afterwards because of the reduced air density at higher altitudes. The design Mach number is reached at an altitude of 128 kft where the unit Reynolds number is computed to be 1.62×10^5 /ft. It seems that the unit Reynolds number used in the aerodynamic design (Ref. [4]) was 2.74×10^5 /ft and this discrepancy is deemed to be the primary cause for the earlier onset of laminarization during flight (i.e., at a Mach number that was significantly lower than the design Mach number of 6).

A large amount of data was acquired during the Pegasus flight. In Section II below, we analyze the thermocouple data to determine the major trends associated with laminar-turbulent transition over the glove and the inboard tile during the flight. Results of the post-flight computational analysis are described next. Specifically, Section III outlines the geometry and the computational procedure used to determine the mean flow at selected times during the flight. An analysis of the relevant aspects of mean flow computations, including a grid convergence analysis and the comparison between computed and measured surface pressure distributions are also presented in this section. Section IV contains the results of linear stability analysis and N factor correlations. Data from the dynamic sensors are discussed in Section V, which provides a comparison of transition onset determined by hot-films and thermocouples. Section VI highlights the major sources of uncertainty in determining the experimentally inferred transition locations as well as in the N-factor correlations based on linear stability calculations. We comment on the spatial extent of the transition region in Section VII and the main findings from this study are summarized in Section VIII.

II. Analysis of Thermocouple Data

Figure 8 shows the typical history of measured temperature for three selected thermocouples along the outboard row (see Fig. 6). These thermocouples are named TOL5, TOU5 and TOU8, respectively, and are located at distances of -12, 11.9 and 22.8 inches, respectively, from the leading edge of the glove. Here, the negative sign indicates a thermocouple location on the lower surface of the glove (as indicated by the letter L within its designation). The temperature history at each thermocouple location shows an initial rise at an approximately constant rate. Between about 48 and 51 seconds into the flight, each temperature curve goes through a bend and then settles again to a new constant, but lower rate of increase. Based on the shape of this bend region, it is referred to as a “knee” from here on for convenience. The glove boundary layer is initially turbulent but eventually becomes laminar as the free stream Reynolds number decreases sufficiently. The existence of the “knee” in a temperature curve is an indication that the boundary layer has laminarized at the location of the given thermocouple. Since the heat transfer rate is higher for a turbulent flow than for the laminar flow, the surface temperature on the glove increases faster with time

when the flow is turbulent than when it is laminar. The time history of the heat flux at the locations directly above thermocouples on the glove surface are plotted in Fig. 9 and the relatively rapid drop in the heat flux clearly indicates transition from turbulent to laminar flow. The heat flux is proportional to the time derivative of the surface temperature, and therefore, the large noise in the heat flux curves is due to differentiation of the non-smooth experimental data. Figure 10 shows the heat flux history along the entire outboard row of thermocouples. Here, the red color indicates high values of heat flux (at earlier times) and blue color indicates low values (at later times). It can be seen that, at just below 50 seconds into the flight, the heat flux undergoes a sharp drop, signifying laminarization of the glove boundary layer in the outboard region.

Henceforth, we will associate the time of transition from turbulent to laminar flow with the location of the "knee" along the temperature history curve. More specifically, the transition point is defined as the point where the temperature curve has the most negative second derivative, as determined numerically via locally parabolic fits to the temperature curves. An analogous procedure may be used to determine the transition point using the heat flux data, except that linear fits are used in lieu of parabolic fitting and the transition point is associated with the most negative value of the slope of these straight line fits.

Figure 11 shows the transition locations over the glove and the inboard tile region as determined using the above procedure. The results are presented in the time–distance domain (where the distance is measured from the leading edge of the glove). There is reasonable agreement between results using the "knee" approach and the heat flux approach, except for the inboard row on the glove which showed larger scatter in the heat flux results for some unknown reason. The one-dimensional heat flux assumption breaks down in the tile region; therefore, only the results based on the "knee" in the temperature curve are shown for the inboard-tile row of thermocouples. The results in Figure 11 indicate that the glove boundary layer is laminar at times above these curves and turbulent at earlier times, *i.e.* below the curves. At time t = 50 seconds, for example, the glove boundary layer transition is expected to occur at 26 inches, 47 inches, 55 inches and 10 inches from the leading edge along the outboard, center, inboard and inboard-tile rows, respectively. In the glove leading edge region, peaks are present in the data processed by the current "knee" analysis, apparently indicating that the attachment-line flow remains turbulent longer than that in the downstream region of the glove. However, as noted below, the above peaks are likely an artifact of the present measurement and/or data reduction technique.

In Figure 12, we plot the same results as in Fig. 11 except using the X-coordinate that is now measured from the wing trailing-edge and increases towards the leading-edge. Only results based on the "knee" in the temperature distribution are plotted. The results from the two extra rows of thermocouples are also included in this figure. The 'Extra 1' row has only three data points. The results of the 'Extra 2' row, which has five thermocouples, stand out from the rest as the transition times for these thermocouples are higher in comparison with the neighboring rows. There is no apparent reason for laminarization to occur at a later time along the 'Extra 2' row except if one postulates the presence of a roughness site somewhere in the neighborhood of the interaction of this row with the leading-edge joint shown in Fig. 2. Such a roughness could precipitate bypass transition and introduce a turbulent wedge within its wake, which would tend to laminarize at a later time than the two neighboring rows. However, the existence of roughness site would be purely speculative as we do not have any information about the detailed in-flight shape of the glove. Pre-flight measurement had shown that the glove surface in the region of the leading edge joint was smooth and the maximum peak-to-valley roughness height was less than 1 micron.

We now consider the transition history inferred from the thermocouple data in the attachment-line region and comment on the peaks noted during the discussion of Fig. 11. In the neighborhood of the leading edge, the glove is constructed from a solid steel block as compared to a thin sheet of steel over the rest of the glove. The solid block construction extends from –2 inches to 4 inches along the lower and upper sides of the leading-edge, respectively. Consequently, the surface temperature computed via the one-dimensional inverse heat conduction problem based on the thin-skin assumption is no longer accurate. Furthermore, the thick steel block also acts as a heat sink, resulting in a reduced rate of temperature rise. For some of the thermocouples located in the leading-edge region, the "knee" in the temperature history curve is barely discernable (see Fig. 13(a)). On the other hand, in the region of inboard tiles (which act as heat insulators), the "knee" in the temperature curve is clearly visible (see Fig. 13(b)). Therefore, transition time for the leading edge tile region can be more readily determined. However, as described below, additional considerations are necessary to estimate the state of the boundary layer near the attachment line.

It was noted above that a turbulent boundary layer may relaminarize in the presence of strong favorable pressure gradients. Therefore, we considered the possibility of a turbulent attachment-line with laminarization downstream due to flow acceleration. The relaminarization criterion was proposed by Narasimha and Sreenivasan [39] for two-dimensional boundary layers and was found to be applicable to swept wing flows by van Dam et al.[37] and Viswanath et al.[40]. According to this criterion, the value of flow acceleration parameter κ_s must exceed 3×10^{-6} for

relaminarization to occur. The values of κ_s computed for the present experiment for t = 50 seconds was found to be about 2×10^{-6} (i.e., less than the critical value). However, as pointed out later, there is large uncertainty associated with computation of this parameter in three-dimensional boundary layers. For the purposes of present study, we will ignore the peaks in the leading edge region in Fig. 11 (see also Fig. 12, where such peaks are more clearly evident) and assume the attachment-line boundary layer to be laminar, provided the downstream boundary-layer is also laminar for a given time during the flight. Transition history just downstream of the leading edge provides an indirect way of determining the state of the attachment-line boundary layer in the absence of relaminarization in the sense of Refs. [39-40].

A close examination of the results presented in Figs. 11-12 would reveal that laminarization at short distances away from the attachment line tends to begin at approximately 47.2 seconds into the flight along the inboard row of thermocouples; transition times along the center and outboard rows are 47.4 and 48.4 seconds, respectively. When laminarization first occurs along the inboard row on the glove, the inboard-tile boundary layer is already laminar over the first 6 inches from the leading edge. This clearly illustrates that laminarization near the leading edge occurs first at the inboard side of the glove/tile region and the transition front propagates along the leading edge towards the outboard side in just over one second, and that the entire attachment-line boundary layer is laminar at about 48.4 seconds into the flight. As noted above, data were also taken by using dynamic sensors located near the rear of the glove. We will discuss these data in a later section. We now turn our attention to the computation of boundary-layer mean flow and N-factor analysis for correlation with thermocouple-based transition data discussed in this section.

III. Computational Results for Mean Flow and Comparison with the Experiment

As stated earlier, the flow past the gloved wing is fully turbulent to begin with. Boundary layer transition (i.e., laminarization in this case) begins to occur after about 47 seconds into the flight and the glove boundary layer becomes fully laminar by t = 55 sec. Accordingly, the experimental conditions at 48, 50, 52, 54 and 56 seconds into the flight have been selected for mean-flow computations using the Navier-Stokes code, CFL3D[41]. The main objective behind the mean-flow computations is to provide high quality boundary-layer profiles over the glove and the tile region, which can later be used for boundary-layer stability analysis and N-factor computations for the purpose of transition correlation. Previous experience with CFL3D indicated that this Navier-Stokes code is able to generate sufficiently accurate mean boundary layer profiles for simple configurations (flat-plate and sharp cone) for which similarity solutions are available for comparison[9, 42].

A. Flow conditions, geometry, and computational procedure

The flight conditions at the times selected for mean flow computation are listed in Table 1 (and also depicted in Fig. 14). These cases cover a range of free stream Mach numbers between 4.13 and 4.99 and unit Reynolds numbers of 1.25×10^6 /ft and 0.56×10^6 /ft, respectively. Computations were performed for 3 different grids (G1, G2, G3), which will be discussed below.

Table 1: ***Free stream and flight conditions of 5 computational cases. The last three columns, G1 through G3, represent respectively the increasingly finer grids, and the thick dot(s) indicates the grid(s) employed during the mean flow computation in each particular case.***

Time(s)	Mach	Alt.(ft)	AOA(deg)	Temp(R)	Re(/ft)	G1	G2	G3
48	4.13	77900	5.94	396.7	1,252,020	•		•
50	4.35	82600	5.95	399.3	1,047,792	•	•	•
52	4.56	87400	5.98	401.9	869,784	•		•
54	4.78	92700	4.27	404.8	705,924	•		
56	4.99	98200	2.52	407.8	556,196	•		•

Figure 15 shows the portion of the vehicle surface used in the present CFD analysis. The bulge on the wing represents the glove/tile region, which is the region of interest for transition analysis. The vehicle tail and the fuselage downstream of the wing are not shown as they were not included in the simulation. Even though the Pegasus vehicle geometry is non-symmetric (on account the glove installation on the starboard side), the effect of this asymmetry was assumed to be small and, hence, the computations modeled only the starboard half of the vehicle, imposing symmetric flow across the center plane of the fuselage. The Pegasus vehicle was also known to have experienced a yaw angle of up to about -1 degree during the time period of interest. However, the effects of this yaw were also ignored after considering the relative trade-off with the increased computational cost required for simulating the full vehicle.

A considerable effort was spent to ensure that the modeled geometry was closely matched with that of the in-flight vehicle configuration. Mr. Carl Rogers of the Geometry Laboratory at NASA Langley Research Center defined the final computational geometry after studying the relevant reports, drawings, visual footage, and discussions with key experimental personnel regarding the design, manufacture, and assembly of the glove.

Three different grids were generated for the mean flow computations. The coarsest multi-block grid consisted of a total of 17.5 million grid cells in 110 grid blocks, of which 15 blocks with a total of about 2.4 million cells were in the glove and tile region on the upper and lower surfaces. The grid in this region was designed so that approximately 70 to 80 cells in directions normal to the wall are used within the boundary layer, at least at surface locations downstream of the wing leading edge region. At the leading edge, there are approximately 50 cells within the boundary layer. Consequently, approximately half a million grid points are used just to resolve the boundary layer over the glove. The vehicle surface is designated by index $K = 1$ for each grid block, *i.e.* it is parameterized by indices *I* and *J*.

In addition, two refined grids were constructed by increasing the number of grid points in the *K*-direction with a total of 28.2 million (medium) and 41.9 million (fine) grid cells, respectively. The medium grid is obtained by adding points in the inviscid region outside the boundary layer to better resolve the nose shock wave and the wing leading-edge shock, while the fine grid was obtained by adding points to both the inviscid region and the viscous region inside the boundary layer, with approximately 110 to 120 points in the boundary layer away from the leading edge region. At the leading edge, there are approximately 90 points within the boundary layer. For convenience, we will refer to these three grids as G1, G2 and G3, respectively, in increasing order of fineness.

A close-up view of the glove/title region and the corresponding surface distribution of grid cells are shown in Fig. 16. In this figure, the grid I-index runs mainly in the streamwise direction; grid J-index mainly in the spanwise direction, converging towards the tip of the delta wing; and grid K-index in the wall-normal direction at the vehicle surface.

Figure 17 shows a representative constant *J*-plane grid over a spanwise section of the glove that is indicated by a yellow line in Fig. 16. Our main objective for performing the CFD computations is to obtain accurate mean flow profiles over the glove and the tile regions and use these profiles for stability analysis. The latter requires the mean flow profiles to be specified on lines perpendicular to the local surfaces of the wing. Thus, in order to facilitate the generation of mean flow files during the post-processing stage (without any extraneous noise associated with multi-dimensional interpolation), the grid lines aligned with the K-direction are designed to be orthogonal to the surface as much as possible. To quantify the degree to which the normal K-grid requirement is satisfied near the surface, numerical tests were carried out to determine the maximum deviation of the *K*-grid line from the surface normal. Specifically, at each grid point (*I*, *J*) on the surface, the surface unit normal vector is determined first. Then the unit vector in the direction of the grid line between *K* and *K*+1 is evaluated. The larger the angle between these two unit vectors, the larger the deviation of the grid line from the surface normal. This is repeated for all grid points within the glove boundary layer. It is found that the maximum deviation is 6.5 degrees, and the average deviation is 0.9 degrees. Thus, for small wall-normal distances (i.e., within the boundary layer), the requirement of wall-normal grid is satisfied to a reasonable degree.

Computations were carried out on the Columbia computer cluster at NASA Advanced Supercomputing (NAS) Center using 64 processors. The required wall-clock time is approximately 5 seconds per iteration for the G1 grid, 8 seconds per iteration for the G2 grid and 12 seconds per iteration for the G3 grid. Solutions appear to converge after approximately 100,000 to 150,000 iterations at the finest level of grid sequencing, depending on the Reynolds number. (In general, higher the value of the Reynolds number parameter, the higher the number of iterations required for convergence.) Typically, the global residual would drop approximately three and half orders of magnitude before settling down to some mean value. A possible and/or partial cause behind the stagnation in residual convergence may be related to weak but persistent spatio-temporal oscillations outside the boundary layer, which were observed for all three grids and in all four cases (t = 48 through 56 seconds), These numerical oscillations start near the attachment line region behind the detached shock wave and are washed over the wing

surface. Away from the attachment line, the oscillations are mostly restricted to regions external to the boundary-layer edge and do not appear to affect velocity profiles inside the boundary layer. Figure 18 shows two sets of velocity profiles, one near the attachment line and the other away from it. The velocity profiles from each set correspond to the same spatial location, but different values of the iteration index. Index 0 denotes an arbitrary instance after the solution had nominally converged. The other two instances correspond to an iteration increment of approximately 15,000 each. Small amplitude oscillations are discernable near the boundary-layer edge.

These oscillations made it difficult to establish a definitive convergence criterion at which to terminate the mean flow computations. Therefore, we let the program run for a large number of iterations even after the residual had settled around some mean value, until the boundary layer profiles had converged sufficiently. It took approximately 14 to 21 days of wall clock time to complete a fine grid case.

As stated earlier, boundary layer transition (laminarization, in this case) begins to occur after about 47 seconds into the flight. While computations have been performed at various times into the flight, the $t = 50$ case is selected for detailed analysis. In particular, the conditions at 48, 50, 52, 54 and 56 seconds are used for the 5 computational cases with the G1 grid (coarse grid). Additional computations are also performed for conditions at 50 seconds with the G2 grid, and for 48, 50, 52 and 56 seconds with the G3 grid.

For CFD computations, no-slip boundary conditions are used throughout the vehicle surface. Surface temperature distribution within the glove and tile regions is derived from the thermocouple measurements. For lack of temperature measurements outside of the glove and tile regions, zero heat transfer condition is imposed over the rest of the vehicle surface. Although the validity of this assumption may be questionable, one expects that the thermal wall boundary condition over the rest of the surface will have a minimal influence on the boundary layer in the region of interest for the present analysis.

As shown in Fig. 6, three main rows (inboard, center and outboard) of thermocouples were provided on the glove, with an additional row in the inboard tile region. Temperature data from these four rows of thermocouples at t = 50 seconds is plotted in Fig. 19. It can be seen that while the tile temperature is much higher than the glove temperature, spanwise variation of the temperature on the steel glove is very small. Therefore, for present computations, linear spanwise variation of temperature is assumed between two adjacent lines of known temperature on the glove.

The temperature variation as a function of distance from the leading edge on the inboard tile is known only along a single row. We therefore assume that the tile temperature varies primarily along the streamwise length of the tile, but may be averaged over the narrow spanwise width of the tile. No measurements are available to specify the surface temperature distribution along the outboard tile. However, since the outboard tile is made of the same material as the inboard tile, it is reasonable to assume that the temperature variation as a function of distance from the leading edge on the outboard tile is similar to that on the inboard tile and this assumption is used in the present computations.

There is a very sharp temperature jump between the glove and the tile regions. To avoid potential numerical difficulties as a result of this jump, moderate smoothing is applied to the specified wall temperature data, by the technique of averaging the neighboring points. The resulting temperature distribution is shown in Fig. 20, where red and blue colors represent the high and low temperatures, respectively, and the green shade indicates an intermediate value of temperature.

B. Mean Flow Results

B.1. Inviscid Region

The main feature of the overall inviscid flow is the nose shock, which is shown in the pressure contour plot in Fig. 21. Also seen are the wing leading edge shock and a much weaker shock that originates at the tip of the triangular shaped wedge (the fillet, see Fig. 1), which extends forward from the leading edge of the wing near the wing-fuselage junction. The wedge shock wave eventually intersects both the wing leading-edge shock and the inboard tile as shown in the more detailed pressure contour plot in Fig. 22. The wedge shock has a pressure ratio of approximately 2.6 (pressure behind the shock to that in front of the shock) just before it intersects the leading-edge shock, while the pressure ratio for the leading-edge shock is approximately 12. The weaker wedge shock does not appear to disturb the boundary layer flow over the inboard tile in any significant manner.

B.2. Streamlines and Friction Lines

The flow in the glove and the inboard-tile regions is of particular interest for the present transition analysis. The inviscid streamlines and the surface friction lines are shown in Fig. 23 for t = 50 case. The streamlines are generally curved inboard, indicating the existence of pressure gradient in that direction, which then induces the crossflow. The friction lines curve even more inwards, confirming the existence of crossflow. Streamlines in Fig. 23 are constructed by using TECPLOT and by assuming the inviscid velocity field to be the velocity field at some constant K-plane (K = 120 from grid G3, in this example). Changing K moderately does not affect the shape of these streamlines. The friction lines are everywhere tangential to the local skin-friction vector on the surface. Therefore, the friction lines shown in the figure are obtained by letting TECPLOT construct "streamlines" based on the computed surface-friction vectors as if they were velocity vectors. The figure also shows the location of inboard and outboard pressure taps and thermocouples. In a few cases, friction lines coming off of pressure taps do tend to cross the outboard thermocouples, but there is no evidence to suggest that the pressure taps tripped the boundary layer, except perhaps for t = 48 seconds.

A three-dimensional perspective of the streamlines and friction lines is shown in Fig. 24, where the depicted geometry includes the glove surface and the inboard tile along with a section of the inboard wing. The attachment line can be seen clearly in the streamline plot on the left. Note that some streamlines that start on the inboard wing enter the tile region, and some streamlines on the inboard tile region enter the glove region. Thus, disturbances that originate in the inboard wing and inboard tile regions may affect transition over the glove. The right side of Fig. 24 shows the surface friction lines, which are everywhere tangential to the local friction vector. These friction lines are released near the attachment line at the same (I, J) locations as the corresponding streamlines (see left part of Fig. 24). It can be noted that, compared with the streamlines, each friction line runs along the leading edge for a shorter distance before turning over to the upper or lower surfaces. This further confirms that there is strong cross flow within the boundary layer. The streamlines and friction lines for the other computed cases are qualitatively similar to the results in Figs. 23-24.

B.3. Boundary-layer profiles

The profiles of velocity and temperature computed for the t = 50 seconds case using the G3 grid (i.e., the finest grid) are shown in Fig. 25. Figure 25(a) shows the velocity profiles in the direction of the inviscid streamline and Fig. 25(b) shows the profiles in the crossflow direction; temperature profiles are shown in Fig. 25(c). The locations of these profiles correspond to selected points along a constant-J line at the midsection of the glove, within the first 4 inches from the leading edge. Visually, all of these profiles (as well as those at downstream locations, not shown here) are smooth, and furthermore, indicate the extent of boundary layer resolution in the mean flow solution.

Figure 26 illustrates the changes in streamwise velocity and temperature profiles at a selected location for all computed cases over the time interval of t = 48 to 56 seconds. Since only the coarsest grid (G1) was used for all of these cases, results presented in the figure are based on this grid. For t = 48, 50 and 52 seconds, it can be seen that the boundary layer thickness increases with t. This is expected because, as indicated in Table 1, the Reynolds number decreases with time while the angle of attack remains approximately the same. For t = 54 and 56 seconds, the boundary layer at the same location appears to get thinner even as the Reynolds number gets smaller. A possible cause for this change may be related to the reduction in angle of attack subsequent to t = 52 seconds (see Table 1 and Fig. 14).

B.4. Effect of grid size on computed results

As described earlier, the three grids (G1, G2 and G3) differ only in the number of grid points in the K-direction. The values of $K_{\max}$ for the three grids are equal to 145, 233 and 345, respectively, and the total number of grid cells are 17.5 million, 28.2 million and 41.9 million, respectively. The G2 grid is obtained by adding points to the G1 grid in the inviscid region outside the boundary layer to better resolve the shock waves, while the G3 grid is obtained by adding points to G1 in both the inviscid region and the viscous region inside the boundary layer.

Figure 27 shows the comparison of experimental and computed pressure coefficients, $C_p = 2\left(p - p_\infty\right)/\rho_\infty U_\infty^2$, along the outboard row of pressure taps at t = 50 and t = 56 seconds into the flight (locations of the pressure taps were shown in Fig. 6). The computational results based on all three grids agree very well with each other. Small differences near the attachment line may be attributed to improved inviscid resolution. Comparison between

computational results and experimental results is also remarkably good, considering that this is perhaps the first ever in-flight measurement of surface pressure at high Mach numbers.

Computed results along the inboard row of pressure taps are presented in Fig. 28 for cases of t = 50 and t = 56 seconds. Again, the agreement among the computed results for these different grids is good. However, comparison with the experimental results is considerably less satisfactory and, furthermore, seems to deteriorate at larger flight times. The computed results show little variation in surface pressure along the spanwise direction and, given the good agreement with measurements from the outboard taps, the reason behind the lack of agreement for the inboard row of pressure ports is not known. The jaggedness of experimental data in Fig. 28, as compared to Fig. 27, seems to suggest that pressure taps along the inboard row may have failed to operate appropriately.

Effect of grid resolution on the computed velocity and temperature profiles along the mid span of the glove is shown in Fig. 29 for t = 50 seconds into the flight. As noted before, computations were carried out for all three grids in this case. Figures 29(a), (b) and (c) show the streamwise, crossflow and temperature profiles, respectively, using the three different grids. The comparison is shown at two streamwise locations (s = 10.62 inch and s = 20.43 in) and in both these cases the G2 solution agrees with the G3 solution much better than the G1 solution, which indicates that we are possibly close to a grid converged result, if not there already. Similar results were obtained for mean flow profiles at upstream locations, except for crossflow velocity very near the attachment-line due to numerical oscillations noted during the discussion of Fig. 18.

A more stringent test for grid convergence would involve a comparison between wall-normal derivatives of the boundary-layer profiles on the various grids used in present computations. Figure 30 shows the first derivatives (wall normal) of the streamwise and crossflow velocities, as well as of temperature, for G1, G2 and G3 solutions. It can be noted that these profiles appears to be smooth and that, in general, the derivatives computed on the G3 grid compare better with those derived from the G2 grid than the derivatives computed for the G1-grid solution, except for very near the wall. We note that the number of points in the boundary layer is essentially the same for G1 and G2 grids.

B.5. Three-Dimensionality of the Flow Field

The three-dimensional nature of the flowfield over the tile and the glove regions is demonstrated in Fig. 31 by plotting the contours of surface pressure, boundary-layer edge Mach number and wall temperature. It can be seen (Fig. 31(a)) that while the pressure-coefficient contours are generally parallel to the leading edge in the outboard region of the glove, the isobars turn significantly as the inboard tile region is approached. The variation in the boundary-layer edge Mach number is also highly three-dimensional as shown in Fig. 31(b). The highest Mach number on the glove is about 3.6 near the trailing edge, which eliminates the possibility of any significant second mode disturbances even for the cold glove surface. The ratio of wall temperature to adiabatic wall temperature is plotted in Fig. 31(c). This ratio is computed using the boundary-layer edge Mach number distribution shown in Fig. 31(b). The values of surface temperature ratio are much smaller on the glove as compared to the tile regions. Bushnell and Malik[43] showed that while crossflow instability is much less sensitive to wall cooling as compared to the first-mode instability, lower surface temperature does tend to reduce crossflow disturbance amplification rates in supersonic boundary layers. Therefore, we expect lower N factors in the glove region as compared to the tile region. Due to the low value of wall temperature ratio on the glove ($T_w / T_{aw} \approx 0.4$), the possibility of first mode disturbances in the glove boundary layer can be ruled out.

B.6. Reynolds Number Variation along Attachment Line

Before we proceed with N-factor analysis of crossflow disturbances, it is appropriate to discuss the state of the attachment-line boundary layer, which is characterized by defining two Reynolds numbers $\overline{R}$ and $\overline{R}^*$, which are relevant in low speed and high speed flows, respectively. For an initially turbulent flow (e.g., contamination from the fuselage) to relaminarize along the attachment line, $\overline{R}^*$ has to be smaller than approximately 245. The definition of $\overline{R}$ is as follows:

$$\overline{R} = \frac{w_e \delta}{\nu_e}$$

where $\delta = \sqrt{\nu_e / (du_e / ds)}$, and du_e / ds being the boundary layer edge velocity derivative in the direction perpendicular to the attachment line and tangential to the wing surface, and υ_e being the boundary-layer edge kinematic viscosity. The Reynolds number $\overline{R}^*$ is defined as

$$\overline{R}^* = \overline{R}\sqrt{\frac{\nu_e}{\nu^*}}$$

where υ^* is the kinematic viscosity computed at a reference temperature (Poll [24]) T^*, which is given by the empirical formula:

$$T^* = T_e + 0.1(T_w - T_e) + 0.6(T_{aw} - T_e)$$

where T_{aw} is the adiabatic wall temperature defined as $T_{aw} = T_e\left(1 + \frac{\gamma - 1}{2} M_e^2 \sqrt{\Pr}\right)$. Here, Pr (=0.72) and γ (=1.4) are the Prandtl number and the ratio of specific heats, respectively.

Figure 32 shows the comparison between the values of $\overline{R}$ and $\overline{R}^*$ for 48 and 50 seconds into the flight. The values of these parameters within the inboard wing and inboard tile regions are approximately the same, as T_e and T^* approach the same values in these regions. However, $\overline{R}^*$ values on the glove are significantly smaller, as compared to $\overline{R}$, due to the colder glove leading edge. Values of $\overline{R}^*$ generally exceed 300 in all three regions (i.e., inboard wing, tile and glove), reaching values as high as 460 and 550 over the tile at t=50 seconds and t=48 seconds, respectively. We note that both the computed velocity distribution in the immediate vicinity of the attachment line and the corresponding values of $\overline{R}$ and $\overline{R}^*$ are influenced by the aforementioned oscillations in the computed basic state. While it is difficult to estimate the resulting error and/or uncertainty in the values plotted in Fig. 32, we examined the $\overline{R}$ and $\overline{R}^*$ distributions at other values of the iteration index as well as plotting the same distributions based on the average solution over a large number of iterations. This scrutiny indicated that the corresponding variations in the attachment line Reynolds number were significantly smaller over the tile region, but excursions of the order of 10% were noted in case of $\overline{R}$ and $\overline{R}^*$ values over the glove region. This also implies that uncertainty in the value of the acceleration parameter κ_s is expected to be about 20%, since κ_s is related to square of δ.

It is known (Poll[24], Arnal et al.[25]) that the attachment line can sustain turbulence if $\overline{R}^*$ exceeds about 245. The observation that the attachment-line is laminar at $\overline{R}^* > 300$ is consistent with the fact that the Pegasus wing sits above the fuselage and, therefore, turbulent fuselage boundary layer is unable to contaminate the boundary layer along the attachment-line (this has been confirmed by plotting the streamlines on the fuselage, not shown here). Experiments (Creel[23], Fujii and Hornung[44], Coleman and Poll[45]) show that, in the absence of such contamination, supersonic attachment-line boundary layer can stay laminar for $\overline{R}^*$ values up to about 500. While there is considerable variation in the computed values of $\overline{R}^*$, this flight experiment appears to lend some support to the above findings based on wind tunnel experiments. However, more accurate computation of the flow field in the leading edge region is needed before we can make a definitive statement with regards to the critical value of $\overline{R}^*$.

IV. Transition Correlations

A. Crossflow Instability and the Effect of Grid Size

The mean flow profiles based on CFL3D solution were analyzed using the compressible linear stability code, LST3D (Malik[46]), which employs a fourth-order accurate compact scheme (Malik[47]) for the solution of the eigenvalue problem. The saddle point method (see Cebeci and Stewartson[48], Malik[46]) was utilized for N-factor computations, which were performed along a trajectory that is tangent to the group-velocity vector since disturbance energy propagates in that direction. The three-dimensional boundary layer can support both stationary and traveling modes of crossflow instability; the latter have higher growth rates according to linear stability theory and, hence, will yield higher N factors.

The crossflow Reynolds number, which provides a measure of crossflow instability, is defined as $R_{cf} = |V|_{\max} \delta_1 / \nu_e$, where $|V|_{\max}$ is the maximum crossflow velocity, δ_1 is the distance from the wall where crossflow velocity reduces to 10% of its maximum, and ν_e is the kinematic viscosity at the boundary-layer edge. It is known that the boundary-layer becomes unstable to crossflow disturbances when R_{cf} is sufficiently high (a value of about 40 is quoted in Ref. [29], based on incompressible computations). Values of crossflow Reynolds number using 3 different grids for t = 50 seconds case are compared in Fig. 33(a), where the results are plotted along group-velocity lines in the mid-span region of the glove. It can be seen that the G3 grid (the finest grid) gives the smoothest result. The relatively high values of the crossflow Reynolds number clearly indicate that the glove boundary layer is unstable to crossflow disturbances. It should be noted that the oscillation in the values of crossflow Reynolds number are linked to the difficulty in determining the characteristic length scale for the coarse grid case and that R_{cf} does not enter into the governing stability equations; hence, these oscillation do not directly influence N factor computations.

Figure 33(b) shows the effect of grid size used in mean flow computations on N-factor results for the t = 50 seconds case. These calculations are for a disturbance frequency of 1 kHz and are initiated near the mid-span section of the glove. The N-factor based on the G1 grid has the smallest value while that based on the G2 grid has the largest value and the result based on the G3 grid lies in between. It can be seen that N-factor results for the two finer grids lie much closer to each other as compared to the N-factor results for the coarsest grid, which is expected based on the velocity and temperature profile comparisons shown in Fig. 29. Regardless of the grid for mean-flow computations, the mean flow profiles used for stability computations were obtained by interpolating the CFD flow field onto a wall normal grid consisting of 81 grid points. Computations were also performed using 41 wall normal points, with little difference in results; however, all of the N-factor results presented below employed 81 grid points.

B. Crossflow N-factors

We now present N-factor results for crossflow disturbances, which are the only disturbances that are expected to be unstable since, as noted before, the cold wall temperatures (relative to adiabatic wall temperature) over the glove region eliminates the possibility of first mode disturbances and the Mach number at the edge of the boundary-layer edge is not high enough for the second mode to be of significance in this case. We now examine the amplification characteristics of stationary (f=0) crossflow disturbances over the tile and the glove regions. Figure 34 shows group-velocity lines, color coded with the computed N-factor values for four different times (t= 48, 50, 52 and 56 seconds). The dimensions shown in the figures are those of the glove alone (i.e., excluding the tile). The locations of the thermocouples are also shown, with the green color indicating a laminar reading and the red color indicating a turbulent reading, based on the method described in Section II. For t = 48 (Fig. 34(a)), the flow near the outer region of the glove is indicated to be fully turbulent. Therefore, transition correlation can be made only for the tile and the inner region of the glove. The computed results indicate that crossflow disturbances do amplify to large N factors (about 16.2) near the glove trailing-edge.

N-factors on the inboard-tile region are also shown in Fig. 34(a). The maximum stationary disturbance N-factor values (which occur in the vicinity of the trailing edge) reach much higher values (about 26.6) on the tile than on the glove. One possible explanation behind the stronger instability of the tile boundary layer could involve the higher surface temperatures over the tile as compared to those over the glove as suggested by Bushnell and Malik[43]. The transition location in the tile region, as indicated by the thermocouples, is much closer to the leading edge when compared with that on the glove. N factor values for correlation with transition in the glove and tile regions will be determined by performing computations for a wider range of frequencies and these results are discussed later in the present section.

Similar N-factor predictions for the t = 50 seconds case are presented in Fig. 34(b). For the inboard, center and outboard rows, the experimentally determined transition locations (between adjacent green and red dots) lie in regions of relatively high N-factors (of order 10). Experimental data from the “extra 2” row are, however, an exception in that the boundary layer there appears to be turbulent even though the N-factors are smaller, and thermocouples on both sides of this row detect laminar flow. One possible explanation for this anomalous behavior could be related to a potential irregularity in the surface geometry (i.e., roughness element) near the leading edge joint that would have introduced a turbulent wedge in its wake, as discussed in Section 2. However, we have no data available to substantiate this speculation. It is to be noted that all five thermocouples along the “Extra-2” row detect turbulent flow and therefore transition location along this row can not be determined for this case.

N-factor traces for t = 52 seconds case are shown in Fig. 34(c). The thermocouple data show that the flow is laminar along all rows over the glove region, except the outboard row, where the flow along the last three thermocouples is turbulent. The maximum N-factor (i.e., near the glove trailing edge) for stationary crossflow disturbances reaches approximately 8.9. The maximum N-factor for the inboard tile region is computed to be in excess of 21 near the trailing edge, but the transition actually occurs fairly close to the leading edge.

Finally, the results for t = 56 seconds case are shown in Fig. 34(d). Here, the thermocouple data show that the flow is completely laminar over the glove region, which is consistent with the fact that the maximum stationary disturbance N-factor on the glove is less than 5.8. In the tile region, however, the maximum N-factor reaches approximately 14.4 near the trailing edge but transition occurs much earlier, at about 1/3 of the way along the tiles.

Correlations between the transition locations determined from experimental data and the computed N-factors have been carried out. For a given time t, the transition location along any row of thermocouples can be inferred from experimental results presented in Fig. 11 or 12. If a horizontal line is drawn through a particular value of t on the time axis, the x-location of the intersection of this line with the experimental data gives the transition location for the particular row of thermocouples. The horizontal line through t = 56 seconds, for example, intersects only the transition curve for the tile row of thermocouples and is above all the other curves. Therefore, it can be concluded that the glove boundary layer is fully laminar for t =56 seconds based on data from the thermocouples.

After the transition location for each row of thermocouples is established, the associated N-factors can be determined by the intersection of the group velocity lines with the location of transition. In order to determine maximum N factors at transition locations, additional computations were performed to cover a wider range of disturbance frequencies and then envelope of all N factor results was constructed in the glove and tile regions. These results are presented in Fig. 35 which shows the constant N-factor lines over the tile and the glove along with the six rows of thermocouples. Fixed N-factor curves plotted in these figures are color coded with the blue-end of the spectrum representing 0 and the red representing high values. The increment in N-factors between a pair of adjacent lines is 1 in both the glove and tile regions. The N factor values at transition locations and the corresponding frequencies are indicated by blue arrows in these figures.

The frequency dependence of N factors at the transition locations for the glove and tile regions is shown in Fig. 36. The values of transition N factors noted in Fig. 35 are obtained from these results. These N factor values are also listed in Table 2. Transition N factors in the tile region vary from 10.6 to 14.1 while the glove region values range from 7.6 to 11.8 considering all rows of thermocouples. The overall range of N factors is from 7.6 to 14.1 for the most amplified traveling disturbances. If we only consider stationary crossflow disturbances, then the N factor values range from 7 to 12.4, as can be discerned from Fig. 36. As discussed before, the transition location cannot be determined along the "extra 2" row for t = 50 seconds case. The N-factor at the location of the first thermocouple in this case is approximately 8. Since flow on both sides of this row of thermocouples was found to be laminar, a turbulent wedge that is characteristic of crossflow induced transition due to localized roughness may have existed in this region of the glove. Note that the curve in Fig. 36(d) is drawn to capture the expected variation of N factor with disturbance frequency. The kink in the computed data is perhaps an indication of the level of uncertainty in our computational procedure.

The frequencies of crossflow disturbances that give rise to the maximum N factors at the transition locations are given in Table 3, for flight times of 48, 50, 52 and 56 seconds. With the exception of t = 56 second case, maximum N factors tend to occur at relatively high frequencies (8 kHz to 15 kHz) in the tile region. The main conclusion to be drawn from results in Fig. 36 is that a wide range of frequencies amplify in the tile boundary layer and the peak is rather broad. In comparison, the most amplified disturbance frequencies in the glove region are lower (1 kHz to 4 kHz), as given in Table 3.

Table 2: Maximum N-factors at Transition Locations.

	t = 48 sec.	t = 50 sec.	t = 52 sec.	t = 56 sec.
Tile	14.1	12.4	11.1	10.6
Inboard	7.6	9.2		
Extra 1	11.8			
Center	11.4	10.0		
Outboard		10.4	8.6	

We know from the thermocouple data presented in Fig. 12 that the tile transition is complete by about 59.5 seconds into the flight. In Figure 37, we plot stationary disturbance N factor results from the above computations at t = 48, 52 and 56 seconds. If these results are extrapolated to t = 60 seconds, then we estimate the maximum

stationary N factor value to be less than 8 at the tile region trailing-edge. This value of N factor appears to be consistent with experimental finding that the tile boundary layer is fully laminar at t = 60 seconds into the flight.

Table 3: Frequencies of Crossflow disturbances with Maximum N-factors at Transition Locations.

	t = 48 sec.	t = 50 sec.	t = 52 sec.	t = 56 sec.
Tile	15,000	8,000	14,000	3,000
Inboard	4,000	1,000		
Extra 1	2,000			
Center	4,000	1,500		
Outboard		3,500	2,000	

Given the relatively large difference between transition locations on the tile and the glove regions, it is possible to infer some information regarding the turbulence spreading angle. In Figure 34(c), it can be seen that the tile boundary layer becomes turbulent at a short distance from the leading edge, while the in-board glove boundary layer remains laminar all the way to the trailing edge. This means that the turbulent tile boundary layer does not contaminate the glove boundary layer. If we draw a line between the first red-colored thermocouple in the tile region and the last thermocouple along the inboard row on the glove, then this line makes an angle of about 6 degrees with the streamline passing through the red dot. This implies that turbulence spreading angle is less than 6 degrees for this supersonic boundary layer. However, it should be noted that there is a small surface discontinuity (i.e., a gap) between the steel glove and the inboard tile region and that the skin friction lines go from the glove to the tile region in this three-dimensional boundary layer. Therefore, the above finding that turbulence spreading angle in less than 6 degrees in the present case is not necessarily relevant to the commonly used turbulence spreading angle criterion of Fischer[49], which is based on two-dimensional boundary layer experiments.

V. Analysis of Data from High Frequency Sensors

High frequency sensors were also employed on the glove to collect transition related data during the flight experiment. The locations and types of the sensors (for which dynamic data were made available to us by A. Bertelrud) are listed in Table 4, wherein the Digital Data Acquisition and Processing System (DAPS) channel connections are also indicated. The X coordinate in this case is measured from the trailing edge of the wing and increases towards the leading edge, as shown in Fig. 6. All sensors have X coordinates smaller than 47 inches indicating that they are situated very close to the trailing end of the glove, which is at X = 40 in. The coordinate Y increases from the line of symmetry of the delta wing. The hot film sensor connected to Channel 5 is the most inboard and the hot film sensors connected to channels 7 and 8 are the most outboard, while the pressure transducers (channels 1 and 3) are located in between. Data sets were taken by these sensors at approximately 100 milliseconds apart. Each set of data consists of approximately 500 samples at 10 microsecond intervals, *i.e.* the sampling frequency of these sensors is 100 kHz and each sampling block extends over approximately 5 milliseconds. Note that no high frequency sensors were provided in the tile region.

Table 4: Locations of Dynamic Sensors

Nearest TC row	Extra 2	Extra 2	Center	Outboard	Outboard
DAPS Channel	1	3	5	7	8
X (in)	45.4	45.0	45.1	46.9	46.9
Y (in)	55.6	55.8	52.1	60.9	60.9
Type	Pressure transducer	Pressure transducer	Hot film	Hot film	Hot film

Here, we will examine the data set from the Channel 5 hot film sensor and compare the results with thermocouple data. Data from other sensors show similar trends albeit with notable differences. However, these details will not be discussed here. Figure 38 shows the raw signals of Channel 5 hot film at three different times during the flight. The horizontal axes show the record number, with the time interval between each pair of consecutive records being equal to 10 microseconds. The vertical axes show the voltage counts, with 0 and 4095 corresponding to the minimum and the maximum voltage, respectively. The top plot shows the signal when the flow is turbulent, being characterized by large amplitude, high frequency oscillations. The middle plot shows the signal when the flow is transitional, with intermittent intervals of large amplitude oscillations. The bottom plot shows whereon trace of large amplitude and high frequency oscillations, indicating that the turbulent flow has now become laminar.

We will first try to infer the transition location by using the change in amplitude of the oscillations and later examine their frequency content. A good measure of the amplitude of the oscillations is the root mean square (*rms*) value or, equivalently, the standard deviation of the signal. The standard deviation of the signal from Channel 5 shown in Fig. 39 as a function of the flight time is represented by a solid curve with circular symbols. To obtain a smoother curve, the standard deviation plotted in the figure was averaged over three data blocks centered over a given instant of time. It can be seen that the standard deviation for earlier flight times is higher than that for later flight times, with a relatively fast drop in between. We will therefore characterize this drop as "transition" (i.e., laminarization). It can be seen that, in this case, the standard deviation virtually vanishes soon after the drop which is what one expects from the raw signal shown in Fig. 38.

The change from turbulent to laminar flow occurs in approximately 3 seconds for this hot film sensor which is close to the center row of thermocouples. Heat flux results from two thermocouples, which are within 3 inches of this hot film sensor, are plotted in Fig. 40(a). It can be seen that the extent of transition based on the heat flux results (49 -52 sec) is also about 3 seconds.

To define a more precise time for boundary layer transition based on the standard deviation, we use the method devised in Section II for determining transition location from the heat flux data. For each point on the standard deviation curve, we fit a straight line through a few neighboring points and define the slope of the fitted line as the slope of the curve at that point. A sharp drop along the curve has a large negative slope; therefore, we will take the point with the largest negative slope as the transition point. The slope of the standard deviation curve is also shown in Fig. 39 as a solid line without symbols. Based on our definition, transition from turbulent to laminar flow at the location of the hot film sensors occurs at approximately t = 53.1 seconds, while transition at the two closest thermocouples occurs at approximately 50.4 and 51.5 seconds, respectively (see Fig. 40(b)). The transition times as determined from the standard deviation analysis are also plotted in Fig. 12. For Channel 5, transition time lags behind that determined by the nearest center-row thermocouple data by approximately 2.1 seconds for the same X location. Thus, while the time extent of the transition process is about the same when measured using thermocouples and the Channel 5 hot film sensor; there is a shift of about 2 seconds between the two results as far as the transition time is concerned. This is not surprising since the dynamic sensor and the thermocouples respond to different flow quantities and it is known that transition onset location is sensitive to the measurement techniques.

Dynamic data for the hot film sensor represented by Channel 7 exhibited a similar trend in that the temporal extent of transition was determined to be about 3 seconds; however, two differences are to be noted. First, the standard deviation does not vanish right after the 'transition' drop and maintains a small value up to about 60 seconds into the flight. Second, more important difference is that the transition time determined by Channel 7 hot film sensor leads that determined by the nearest outboard-row thermocouple data by about 2 seconds (see Fig. 12). The reason for this differing behavior of Channel 5 and Channel 7 hot film sensors with respect to the thermocouple data is unknown.

The above analysis is based purely on the amplitudes of the oscillations without considering the frequency information. This means that, as an extreme example, a signal of large amplitude, pure sine wave could be construed as turbulence. Therefore, we will next analyze the frequency information derived from the signals.

The power spectral density (indicative of the energy spectrum) of channel 5 hot film signal is shown in Fig. 41. High frequency structures fill the spectrum before t = 54. Beyond this, large amplitude, low frequency waves of up to about 3 kHz remain for some time but eventually they too disappear, which is consistent with the raw signal plots in Fig. 38. Therefore, for the channel 5 data, both amplitude and frequency considerations confirm that transition did occur. We recall that crossflow disturbances with frequencies up to about 4 *kHz* do amplify in the glove boundary layer, according to the stability computations described in Section IV.

VI. Uncertainties in Experimental Transition Locations and Computed N-Factors

We now address the uncertainties in both the transition locations determined from experimental data and the N-factor predictions based on stability computations. As far as the determination of transition location is concerned, there are two types of uncertainties that need to be distinguished. The first type is related to the difficulties in determining the transition location from a given measurement technique. The second type is associated with the differences in transition location based on different physical properties of the flow.

A major uncertainty in correlating N-factors to transition locations is related to the saw-tooth pattern (Dagenhart et al.[50]) associated with stationary crossflow transition. Since the average of the saw-tooth front can only be determined with a sufficiently dense array of thermocouples (or, alternatively, some form of global visualization of the transition front), we are not able to determine if transition in flight was dominated by stationary crossflow modes and, if so, the extent of spatial variations associated with the saw tooth pattern (which amounts to an uncertainty in the transition location determined with a sparse array of instrumentation).

The first type of uncertainty:

The determination of transition location based on the "knee" of the temperature history data was discussed in Section II. The transition process occurs over a finite time interval. For example, in Fig. 8, the flow is turbulent to the far left of the figure and laminar to the far right and transition takes place somewhere between t = 48 and 51 seconds. The "knee" approach associates the transition location with the largest curvature in the temperature history and, hence, the predicted transition location is expected to be in the middle of the transition region. Since the N factor method employs linear stability theory, it is customary to correlate with the location where the flow begins to depart from laminar state but that location is more difficult to determine from the data at hand. Therefore, we chose to correlate N factors with the location in the middle of the transition region (determined from the "knee" approach) knowing that the associated uncertainty is no more than 1.5 seconds, since the transition period is determined to be about 3 seconds. We also note that transition in the present case where Pegasus rocket is ascending is actually relaminarization of the flow from the initial turbulent state, while for reentry vehicles (cf. Malik [9]) the state of the boundary layer changes from laminar to turbulent as the vehicle descends. It is not known if there is a hysteretic effect associated with transition in these cases.

The second type of uncertainty:

We have utilized three different approaches to determine the transition time: the "knee" in temperature history, wall heat-flux and the standard-deviation. The first two approaches are closely related as they both use thermocouple data and, hence, give similar results (Fig. 11); however, the third approach uses data from dynamic sensors that are sensitive to different flow quantities than the thermocouples. As a consequence, the latter sensors are expected to yield a different transition location. In Figure 6 the nearest row of thermocouples to each of the high frequency sensors can be found, and comparing the transition time for each individual sensor with that along its nearest row of thermocouples (Fig. 12), the difference is approximately 2 seconds, which gives a measure of the uncertainty associated with the measurement technique.

The uncertainty in N-factors:

If uncertainty in determining the transition time is about 2 seconds, then the question is how this uncertainty affects the value of N factors. The Pegasus vehicle accelerates as it climbs and in 2 seconds, e.g. from t = 50 to 52, the Mach number increases by 0.21 and the Reynolds number drops by approximately 17 percent. We have computational results available for cases $t = 50$ and $t = 52$ seconds and, therefore, we can comment on the uncertainty in the values of N-factors. We selected three thermocouples nearest to the locations of the high frequency sensors connected to DAPS channels 3, 5 and 7, respectively (Fig. 6), and determined the associated N-factors for traveling crossflow disturbances of *1 kHz* frequency. The results are given in Table 5 below.

Table 5: Maximum N-factors at specified locations and associated frequencies.

DAPS channel	Nearest T.C.	Separation (in)	$N_{t=50}$	$N_{t=52}$
3	Extra2 5	3.31	10.4 (2.0 kHz)	9.0 (1.7 kHz)
5	Center 16	2.97	10.4 (1.5 kHz)	9.1 (1.5 kHz)
7	Outboard 13	1.77	11.3 (2.4 kHz)	8.8 (1.9 kHz)

The N-factors shown in the above table are not N-factors at transition, but those at the three particular locations over the glove, at two particular times separated by 2 seconds. These results show how much the N-factor at a fixed location (which is near transition) can change within this time interval (i.e., by a maximum of 2.8). It was noted that complete laminarization occurs 1.5 seconds after the transition time determined by the "knee" approach. Therefore, N factor values at the complete laminarization time will be lower by about 2 than those computed at the transition time determined by the "knee" approach.

There exist other factors that may give rise to additional uncertainty in the N-factor correlations. For example, the Pegasus vehicle experienced a yaw angle of up to -1 degree during the flight period of interest, but this has not been accounted for in the present computations. This impact associated with this approximation is expected to be small.

Finally, we note that the N-factor method only constitutes an empirical correlation based on linear stability analysis; the actual transition process involves nonlinear growth and secondary instabilities (Malik et al.[30], White and Saric[32]) and, for its prediction, requires detailed knowledge of surface finish and external disturbances as well as the attendant receptivity mechanisms.

VII. Spatial Extent of Transition

After the boundary layer in the leading edge region has been laminarized, it re-transitions to turbulence owing to the growth of crossflow disturbances. The spatial extent of this transition at a given time during Pegasus's flight can be estimated by examining the heat flux distributions along the rows of thermocouple. As noted earlier, heat flux data from the inboard row are problematic; therefore we will only examine data from the center and outboard to investigate length of the transition region. Since the computed heat flux data are oscillatory (*e.g.* see Figure 9), we first smoothed the time history of the heat flux for each individual thermocouple by weighted averaging of neighboring points (in time) for a number of iterations. This is equivalent to applying a low-pass filter to the heat flux data. Then, we constructed plots of heat fluxes versus thermocouple locations in terms of their distances from the leading edge. Figures 42(a) and (b) show heat flux distributions at flight times of approximately 48, 49, 50, 51 and 52 seconds along the center and outboard rows, respectively. The short arrows in Figure 42 point to the transition locations determined by the "knee" approach in the temperature history, as in Fig. 11. It can be seen that heat flux rises as the flow along a particular row under goes transition. For the center row, the first four curves experience such rise, but the last one for $t = 52$ second does not, because flow along the entire row has already laminarized by this time. The distance between the beginning and end of the heat flux rise is the spatial extent of transition. For the center row, this length varies from 15 to 30 inches. For the outboard row, the flow is entirely turbulent at $t=48$ second, but for the other four cases heat flux increases through the transition region as expected. The rise in this case is better behaved as compared to the center row, in that all the curves have relatively flat slopes before and after transition, making the extent of the heat flux rises easier to estimate. The spatial extent of transition for the outboard row is found to be between 9 and 15 inches.

Another approach to determine the spatial extent can also be employed. In Figure 11 the inverse of the slope of each transition curve in the time-versus-distance plot gives the speed at which transition front moves downstream along a particular thermocouple row. As discussed earlier, transition at a fixed location takes approximately 3 seconds to complete. This gives a characteristic time for transition. The product of the characteristic transition time and transition-front speed gives an estimate of the spatial extent of transition. By linear curve fitting using data from 20 to 60 inches and from 20 to 40 inches from the leading edge for the center and outboard rows, respectively, the transition-front speeds are estimated from curves in Figure 11 to be approximately 8 and 4 inches per second for center and outboard rows, respectively, and therefore the transition extents are approximately 24 and 12 inches for the respective rows, consistent with estimates made above from heat flux curves. The ratio of the location of end of transition to the beginning of transition varies from case to case but is close to 1.5 for the outboard row. The location of beginning of transition can not be clearly discerned for the center row, but it seems that the transition extent ratio along this row may be as high as 2 for the t = 49 seconds case. However, it should be noted here that the distance is measured along the thermocouple rows, which are not aligned with the streamlines.

VIII. Summary & Concluding Remarks

The Pegasus flight experiment[1-4] has provided unique laminar-turbulent transition data in three-dimensional boundary layers in the flight Mach number regime of 4 to 5. Thermocouples were used to detect transition on the wing glove constructed from steel as well as on the inboard thermal protection tiles. Hot films and dynamic pressure sensors were provided near the trailing edge of the glove to detect high frequency oscillations within the

boundary layer. Two rows (inboard and outboard) of surface pressure probes were also provided to measure the steady surface pressure at discrete locations on the glove.

The experiment was performed as the rocket was ascending and the initially turbulent boundary-layer began to laminarize beyond a flight altitude of approximately 78,000 feet. Based on the thermocouple data, transition from the initially turbulent to fully laminar boundary layer was complete in approximately 8 seconds over the glove region and about 13 seconds along the row of thermocouples in the inboard tile region. At the location of a given hot film sensor, the turbulent-laminar transition process took about 3 seconds, and approximately same duration for transition was also evident in the data from the nearby thermocouples; however, the time of transition inferred from the hot film data differed from the time based on thermocouple data by approximately 2 seconds.

Mean flow computations have been performed using the CFL3D code, wherein the flow past the Pegasus vehicle was simulated with up to 41 million grid points with particular attention paid to the glove and the surrounding tile region. Effect of grid resolution was also studied by coarsening the grid and the suitability of using the computed mean flow for a linear stability analysis was addressed.

Computed results are in excellent agreement with the measured surface pressure along the outboard row of pressure probes. However, the agreement is less satisfactory along the inboard row and this lack of agreement becomes more pronounced with increasing flight time, at least for the cases computed in this study. The reason for this disagreement along the inboard row could not be established, particularly since computations show relatively small spanwise variation and yield remarkably good agreement with the data from the outboard row of pressure probes.

Since the 45 degree swept delta wing was mounted on top of the Pegasus vehicle, the fuselage boundary layer did not contaminate the wing attachment-line boundary layer. Therefore, the attachment line became laminar even though the Reynolds number parameter $\overline{R}^*$ was above the critical value of 245 for transition due to turbulence contamination. Computational data suggests that the attachment line flow was stable for $\overline{R}^*$ of about 300. However, we note that there is a large uncertainty (about 10 percent) associated with computed values of $\overline{R}^*$ owing to the numerical oscillations in CFD results in the leading edge region.

Linear stability computations showed that the three-dimensional boundary layer was unstable to stationary and traveling crossflow disturbances. The tile boundary layer was unstable to disturbances with a wider range of frequencies as compared to the glove boundary layer. For the cases computed herein, the most amplified disturbance frequency in the tile boundary layer varied from 3 kHz to 15 kHz. The most amplified frequencies in the glove boundary layer ranged between 1 and 4 kHz, which is consistent with the dynamic data from the hot film sensors. The glove boundary layer was found to be less unstable than the tile boundary layer, which is consistent with the experimental finding that, at a given altitude, transition was much further downstream on the glove as compared to that over the tiles. It is suggested that this is primarily due to the lower wall temperature in the glove region as compared to the tile region.

Linear stability analysis for t = 48, 50, 52 and 56 seconds into the flight shows that both stationary and traveling crossflow disturbances attain relatively large N-factors at transition locations determined from the thermocouple data. The values of transition N factors associated with most amplified traveling disturbances vary between 7.6 and 11.8 for the glove boundary layer, and between 10.6 and 14.1 for the tile boundary layer. The corresponding N factor values for stationary crossflow disturbances range between 7 and 11.2 for the glove and between 8 and 12.3 for the tile boundary layer.

Finally, spatial extent of transition has been determined from the thermocouple data. Analysis of the data indicates that transition region is longer along the centerline row of thermocouples as compared to that along the outboard row. The ratio of the location of end of transition to the beginning of transition is found to be about 1.5.

Acknowledgements

The authors would like to thank Dr. Arild Bertelrud of Analytical Services & Materials, Principal Investigator of the Pegasus flight experiment, for providing raw data and data processing code as well as several valuable discussions. This study could not have been completed without his assistance. The authors would also like to extend their appreciation to Mr. Bryan Baldwin of Orbital Sciences who provided information about Pegasus vehicle and wing geometry. Thanks are also due to Drs. P. Balakumar and R. Thompson of NASA Langley who performed preliminary computational analysis of the data. In addition, we thank Mr. Carl Rogers for constructing the computational geometry and Mr. Victor Lessard for generating the CFD grids. Finally, we would like to acknowledge Dr. Ajay Kumar, Director for Systems Analysis and Concepts Directorate, for his encouragement and

support of this work. He provided seed funds to initiate this analysis when he was Director for Aerodynamics, Aerothermodynamics and Acoustics Competency. Without his initiative, this work would not have even started.

References

[1]Bertelrud, A., de la Tova, G., Hamory, P. J., Young, R., Graves, S. S., Diamond, J. K., Noack, R., and Knoblock, D., "Pegasus Wing-Glove Experiemnt to Document Hypersonic Crossflow Transition---Measurement System and Selected Flight Results", AIAA paper 2000-0505, 2000.

[2]Bertelrud, A., de la Tova, G., Budd, G.B., Noffz, G.K., Richards, W.L. and Monaghan, R.C. , "Pegasus Wing-Glove Experiment to Document Crossflow Transition ---- Development and Current Status", AIAA paper 1998-1522, 1998.

[3]Bertelrud, A., Graves, A. S., Young, R. and Anderson, B., "Documentation of Crossflow Transition in Flight at Hypersonic Mach Numbers", AIAA paper95-606, 1995.

[4]Godil, A., and Bertelrud, A, "Design of a Wing Shape for Study of Hypersonic Crossflow Transition in Flight", Computing Systems in Engineering, Vol. 3, pp. 115-130, 1992.

[5]Reshotko, E. "Progress, Accomplishments and Issues in Transition Research", AIAA Paper 97-1815, 1997.

[6]Smith, A. M. O., "Transition, Pressure Gradient and Stability Theory", Proceedings of the International Congress of Applied Mechanics, Brussels, 1956, pp. 234-244.

[7]Mack, L. M. "Boundary Layer Stability Theory", Report 900-277, Rev. A, Jet Propulsion Laboratory, Pasadena, CA, November 1969.

[8]Malik, M. R., "Prediction and Control of Transition in Supersonic and Hypersonic Boundary Layers." *AIAA Journal* Vol. 27, 1989, pp. 1487-1493.

[9]Malik, M. R., "Hypersonic Flight Transition Data Analysis Using Parabolized Stability Equations with Chemistry Effects" *J. of Spacecrfat and Rockets* 40,2003, pp. 332-344.

[10]Chen, F.-J., Malik, M. R. and Beckwith, I. E., "Boundary-layer transition on a cone and flat plate at Mach 3.5." *AIAA Journal* Vol. 27, 1989, pp. 687-693.

[11]Horvath, T. J., Berry, S. A., Hollis, B. R., Chang, C.-L., and Singer, B. A., "Boundary Layer Transition On Slender Cones In Conventionaland Low Disturbance Mach 6Wind Tunnels," AIAA Paper-2002-2743, 2002.

[12]Marshall, L. A. "Summary of transition results from the F-16XL-2 supersonic laminar flow control experiment." AIAA paper 2000-4418, 2000.

[13]King, R.A., "Mach 3.5 Boundary-Layer Transition on a Cone at Angle of Attack", AIAA Paper 91-1804, 1991.

[14]Cattafesta, L. N., III, Iyer, V. , Masad, J. A., King, R. A. and Dagenhart, J. R. 1995 "Three-dimensional boundary-layer transition on a swept wing at Mach 3.5." *AIAA Journal* Vol. 33, 1995, pp. 2032-2037.

[15]Cattafesta, L. N., "Swept-Wing Suction Experiments in the Supersonic Low-Disturbance Tunnel", High Technology Corporation Report No. HTC-9605, 1996.

[16]Hall, P., Malik, M. R., and Poll D. I. A., "On the Stability of an infinite Swept Attachment-line Boundary Layer." *Proc. R. Soc. Lond.* A395, 1984, pp. 229-245.

[17]Lin, R.-S., Malik, M. R., "On the Stability of Attachment-line boundary Layers Part 1. The Incompressible Swept Hiemenz Flow." *J. Fluid Mech.* Vol. 311, 1996, pp. 239-255.

[18]Lin, R.-S., Malik, M. R., "Stability and Transition in Compressible Attachment-Line Boundary-Layer Flow", SAE Technical Paper No. 952041, Aerotech '95, Los Angles, CA, September 18-21, 1995.

[19]Theofilis, V., Fedorov, A., Obrist, D., and Dallmann, U., "The Extended Gortler-Hammerlin Model for Linear Instability of Three-Dimensional Incompressible Swept Attachment-Line Boundary Layer Flow", *J. Fluid Mech.*, Vol. 487, 2003, pp. 271-313.

[20]Coleman, C. P., Poll, D.I.A., and Lin, R.-S., "Experimental and Computational Investigation of Leading Edge Transition at Mach 1.6", AIAA Paper 97-1776, 28th AIAA Fluid Dynamics Conference, June 29-July 2, 1997.

[21]Pfenninger, W. and Bacon, J. W., "Amplified Laminar Boundary Layer Oscillations and Transition at the Front Attachment Line of a 45^o Flat-nosed wing with and without boundary Layer Suction", Viscous Drag Reduction, ed. C. S. Wells, Plenum, 1969.

[22]Poll D. I. A., "Some Observations of the Transition Process on the Windward Face of a Long Yawed Cylinder." *J. Fluid Mech.* Vol. 1501996, pp. 329-356.

[23]Creel, T. R., Beckwith, I. E. and Chen, F.-J., "Transition on Swept Leading Edges at Mach 3.5", *Journal of Aircraft*, Vol. 25, 1987, pp. 710-717.

[24]Poll, D. I. A. "The Development of Intermittent Turbulence on Swept Attachment Line including the Effects of Compressibility", The Aeronautical Quarterly, Vol. XXXIV, February 1983. pp. 1-23.

[25]Arnal, D., Vignau, F., and Juillen, J. C., "Boundary Layer Tripping in Supersonic Flow", *Laminar-Turbulent Transition,* edited by D. Arnal and R. Michel, Springer-Verlag, Berlin, 1990.
[26]Murakami, A., Stanewsky, E., and Krogmann, P., "Boundary-Layer Transition on Swept Cylinders at Hypersonic Speeds", *AIAA Journal*, Vol. 34, No. 4, 1996, pp. 649-654.
[27]Poll, D. I. A. and Danks, M. "Relaminarization of the Swept Wing Attachment-Line by Surface Suction", *Laminar-Turbulent Transition,* edited by R. Kobayashi, Springer-Verlag, Berlin, 1995.
[28]Gregory, N., Stuart, J. T. and Walker, W. S., "On the Stability of Three-Dimensional Boundary Layers with Applications to Flow due to a Rotating Disc." *Phil. Trans. R. Soc. Lond.* A 248, 1955, pp. 155-199.
[29]Malik, M. R., Li, F. and Chang C.-L., "Crossflow Disturbances in Three-Dimensional Boundary Layers: Non-linear Development, Wave Interaction and Secondary Instability." *J. Fluid Mech.* Vol. 268, 1994, pp. 1-36.
[30]Malik, M. R., Li, F. Choudhari, M. M. and Chang C.-L., "Secondary Instability of Crossflow Vortices and Swept-wing Boundary-layer Transition." *J. Fluid Mech.* Vol. 399, 1999, pp. 85- 115.
[31]Kohama, Y., Saric, W. S., and Hoos, J. A., "A High Frequency, Secondary Instability of Crossflow Vortices That Leads to Transition.". *Proc. R. Aeronaut. Soc. Conf. on Boundary-Layer Transition and Control*, Cambridge, UK, 1991, 4.1.
[32]White, E. B. and Saric, W. S., "Secondary Instability of Crossflow Vortices." *J. Fluid Mech.* Vol. 525, 2005, pp. 275-308.
[33]Itoh, N., "Simple Case of the Streamline-Curvature Instability in Three-Dimensional Boundary Layers", *J. Fluid Mech.*, Vol. 317, 1996, pp. 129-154.
[34]Mueller, B. and Bippes, H., "Experimental Study of Instability Modes in a Three-Dimensional Boundary Layer", AGARD CP-438, Paper No. 13, 1988.
[35]Mack, L. M., "Linear Stability Theory and the Problem of Supersonic Boundary-Layer Transition", *AIAA Journal*, Vol. 3, 1975, pp. 278-289.
[36]Saric, W. S. and Reed, H. L., "Supersonic laminar flow control on swept wings using distributed roughness." AIAA paper 2002-147, 2002.
[37]Van Dam, C. P., Vijgen, P. M. H. W., Yip, L. P. and Potter, R. C., "Leading-edge Transition and Relaminarization Phenomena on A Subsonic High-Lift System", AIAA Paper 93-3140, 1993.
[38]Beck, J. V., Blackwell B., ST. Clair, C. R. Jr., "Inverse heat Conduction: Ill-posed Problems," John Wiley & Sons, Inc. 1985, pp-13-15.
[39]Narasimha, R., and Sreenivasan, K. R., "Relaminarization in Highly Accelerated Turbulent Boundary Layers", Journal of Fluid Mechanics, Vol. 61, pp. 417-447, 1973.
[40]Viswanath, P. R., Mukund, R., Narasimha, R. and Crouch, J. D., "Relaminarization on Swept Leading Edge under High-Lift Conditions", AIAA Paper 2004-99, 2004.
[41]Krist, S., Biedron, R.T., and Ramsey, C.L., "CFL3D User's Manual (version 5.0)", NASA TM-1998-208444, 1998.
[42]Garriz, J. A., Vatsa, V. N., and Sanetrik, M. D., "Issues Involved in Coupling Navier-Stokes Mean Flow and Linear Stability Codes", AIAA Paper No. 94-0304, AIAA Aerospace Sciences Meeting, Reno, Nevada, January 10-13, 1994.
[43]Bushnell, D.M. and Malik, M.R., "Supersonic Laminar Flow Control", *Research in Natural laminar Flow and Laminar-Flow Control, NASA CP 2487,* compiled by J. Hefner and F. Sabo , 1987.
[44]Fujii, K. and Hornung, H.G., "Experimental Investigation of High-Enthalpy Effects on Attachment-Line Boundary-Layer Transition", *AIAA Journal*, Vol. 41, No. 7, July 2003, pp. 1282-1291.
[45]Coleman, C. P. and Poll, D.I.A., "Roughness-Induced Attachment-Line Transition on a Swept Cylinder in Supersonic Flow", *AIAA Journal*, Vol. 39, No. 4, pp. 590-596, 2001.
[46]Malik, M. R., "Boundary-Layer Transition Prediction Toolkit", AIAA Paper 97–1904, 28th AIAA Fluid Dynamics Conference, Snowmass Village, CO, June 1997.
[47]Malik, M.R., "Numerical Methods for Hypersonic Boundary Layer Stability", *J. Comp. Phys*, Vol. 86, No2, pp. 376-413, 1990.
[48]Cebeci, T. and Stewartson, K., "On Stability and Transition in Three-Dimensional Flows", AIAA J., Vol. 18, pp. 398-405, 1980.
[49]Fischer, M. C., "Spreading of a Turbulent Disturbance", AIAA J., Vol. 10, No. 7, pp. 957-959, 1972.
[50]Dagenhart, J. R., Saric, W. S., Hoos, J. A., and Mosseux, M. C., "Experiments on Swept- Wing Boundary Layers", In Laminar-Turbulent Transition (Eds. D. Arnal and R. Michel), vol. 3, pp. 369-380, Berlin: Springer Verlag, 1990.

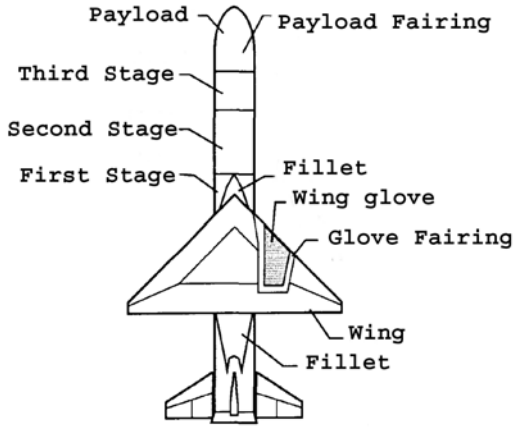

Figure 1. Plan view and layout of the baseline Pegasus launch vehicle with the wing glove (from Ref. [1]).

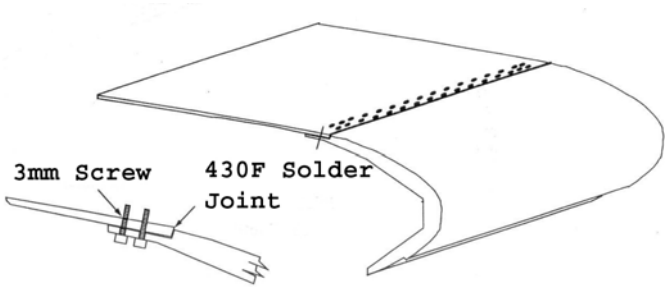

Figure 2. The joint between the leading edge block and the thin steel sheet.

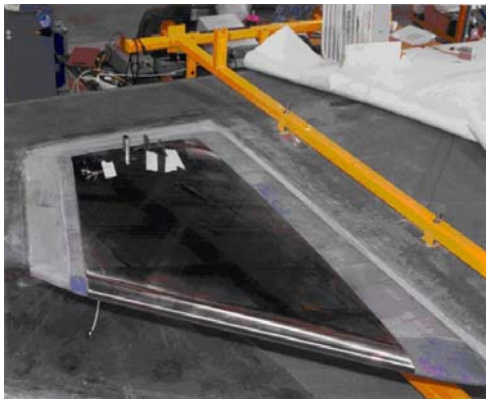

Figure 3. Photograh of the glove embedded within ceramic tile boundary.

Figure 4. Preflight photograph of the glove assembly.

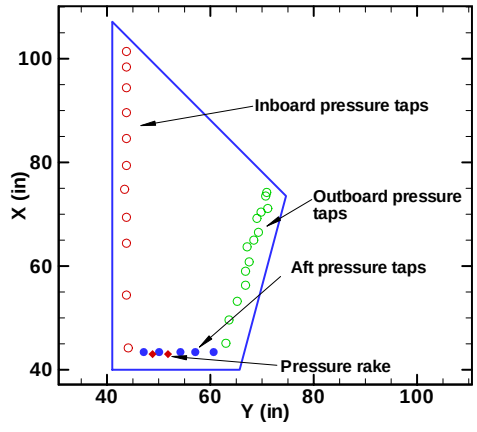

Figure 5. Locations of pressure taps on the glove.

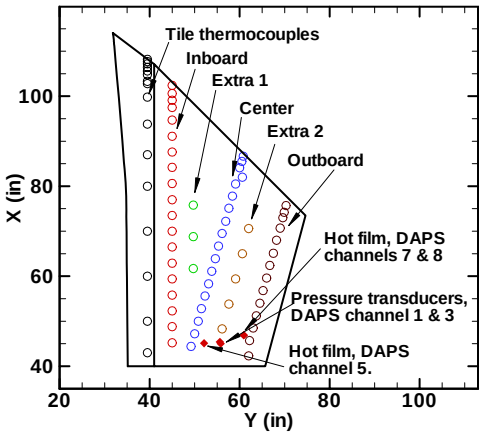

Figure 6. Locations of thermocouples and high frequency sensors.

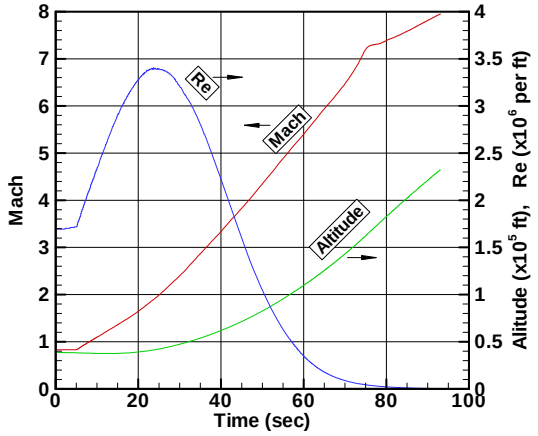

Figure 7. Unit Reynolds number, altitude and Mach number history.

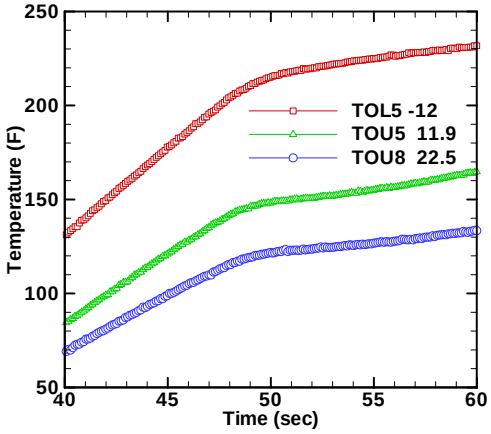

Figure 8. Typical temperature history from thermocouple data.

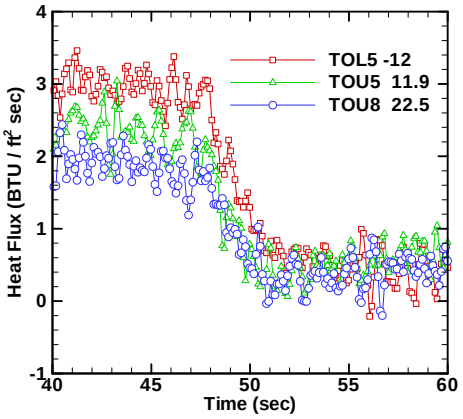

Figure 9. Typical heat-flux histories derived from thermocouple data.

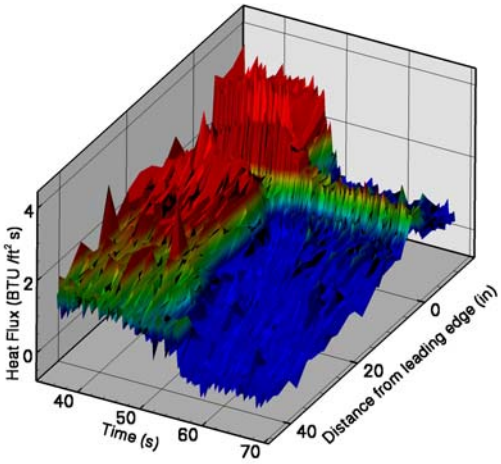

Figure 10. Heat flux history along the entire outboard row of thermocouples.

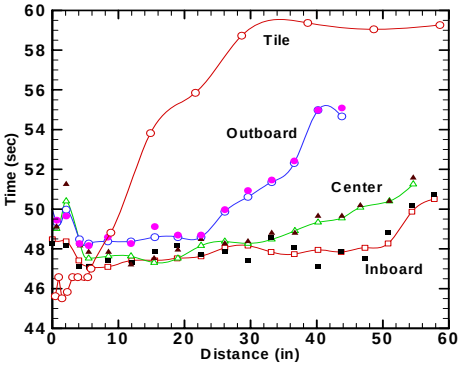

Figure 11. Transition locations based on temperature 'knee' (line with hollow symbols) and heat-flux data (solid symbols). The region above a curve indicates laminar flow and that below it to be turbulent.

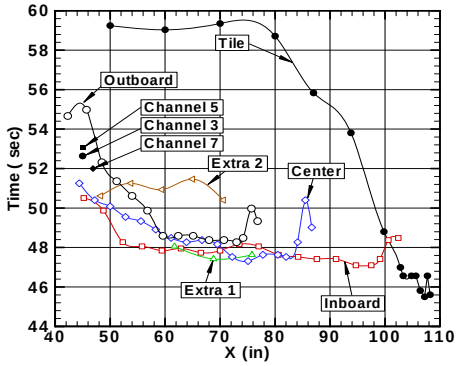

Figure 12. Same as Fig. 11, except X is measured from trailing edge of the wing, pointing upstream. Also included are transition data from two auxiliary rows of thermocouples and the high frequency sensors.

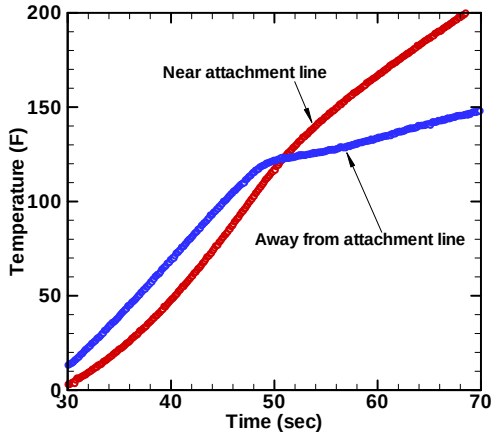

(a) glove

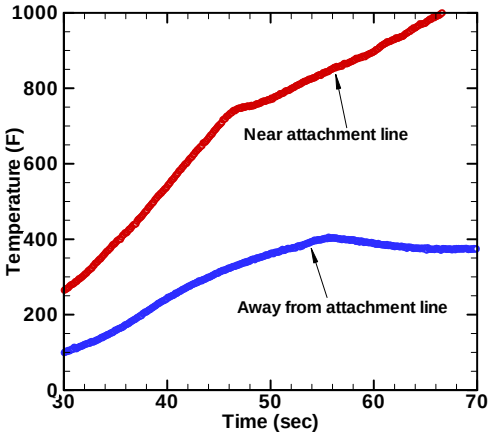

(b) tile

Figure 13. Comparison of temperature histories of thermocouples near the attachment line and away from it. Left: on the glove, right: in the tile region.

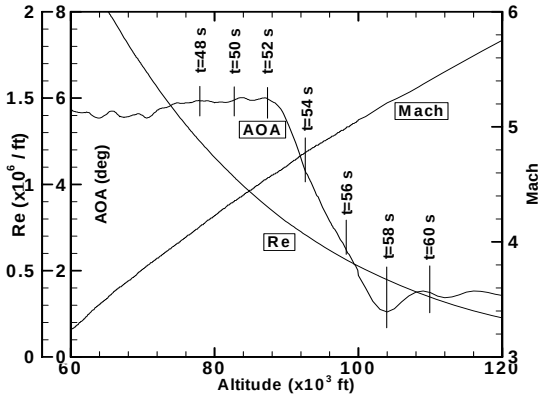

Figure 14. Unit Reynolds number, angle of attack and flight Mach number.

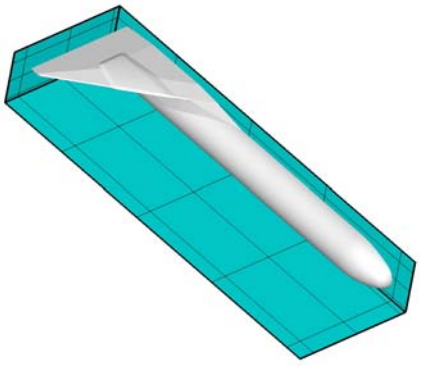

Figure 15. Surface of the half Pegasus vehicle. The bulging part on the wing is the glove/tile region.

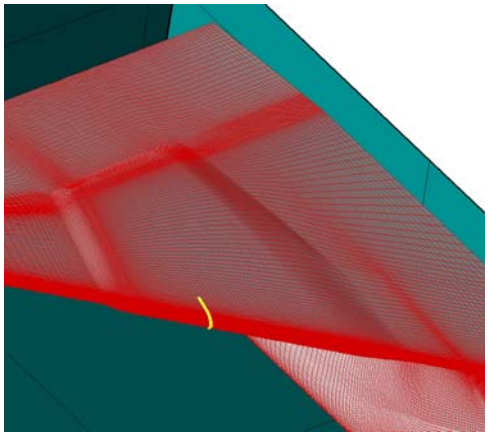

Figure 16. Surface grid distribution. The wall-normal grid along the yellow line is shown in Fig. 17.

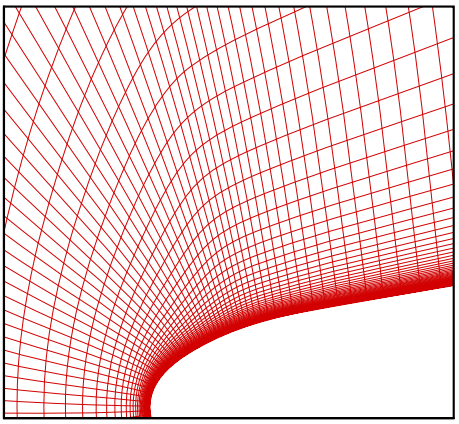

Figure 17. Grid lines normal to the surface.

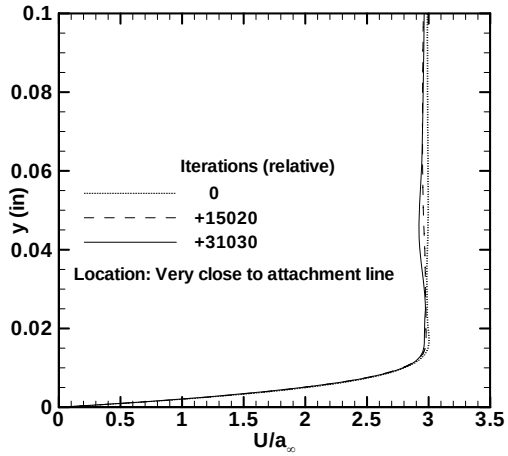

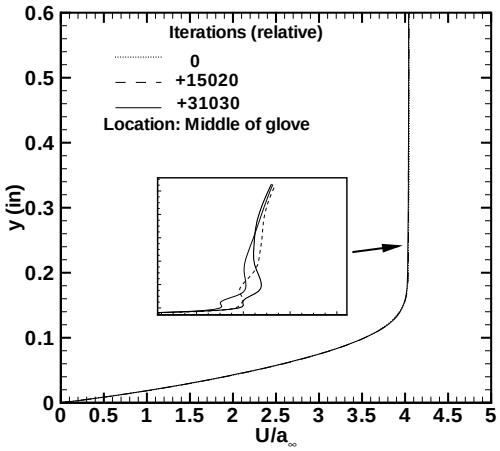

(a) Close to attachment line *(b) Middle of glove*

Figure 18. Streamwise velocity profiles showing oscillations near the boundary-layer edge.

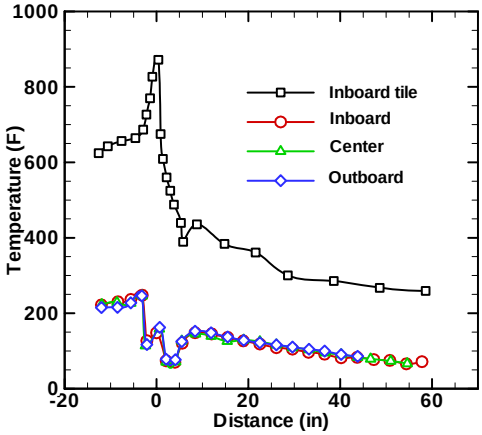

Figure 19. Thermocouple data in the inboard-tile and glove regions (inboard, center and outboard rows).

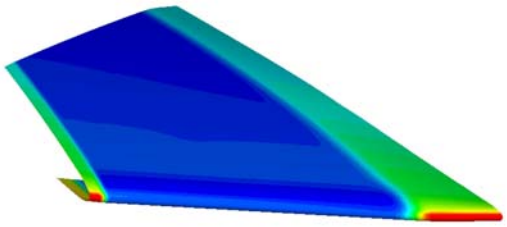

Figure 20. Temperature distribution over glove/tile regions used in CFD computations . Red, green and blue colors indicate, respectively high, medium and low temperatures.

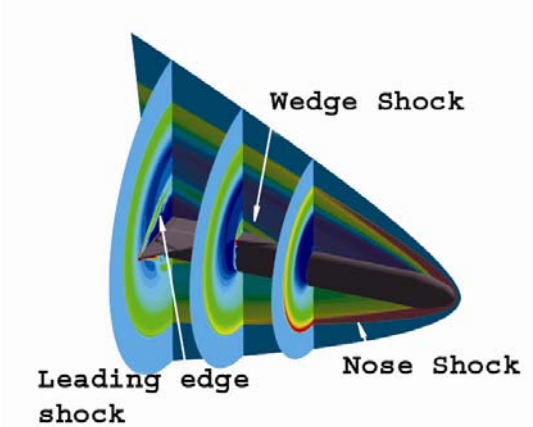

Figure 21. Pressure contours showing the three shocks captured in CFD computations.

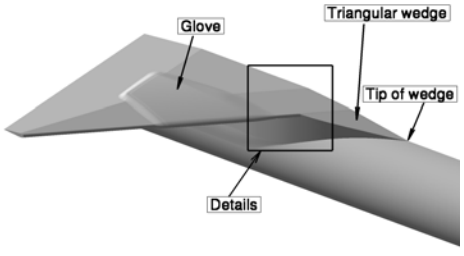

Figure 22 (a). Wing and fuselage assembly; region of detail is shown in Fig. 22(b).

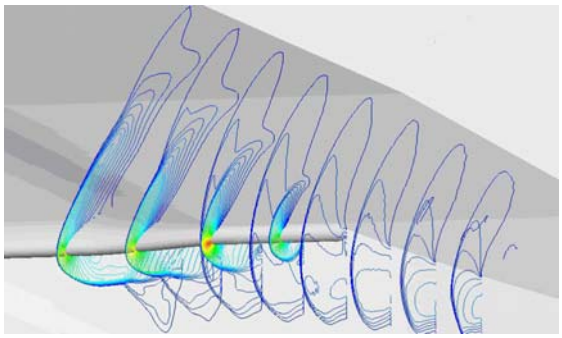

Figure 22 (b). Pressure contour showing the details of the intersection of the wedge shock and the wing leading-edge shock.

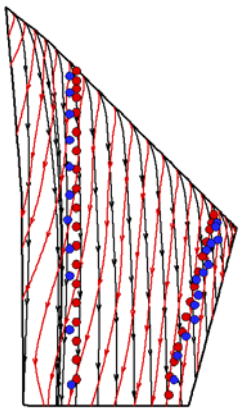

Figure 23. Streamlines (black) and friction lines (red) along with locations of inboard and outboard thermocouples (red) and pressure taps (blue).

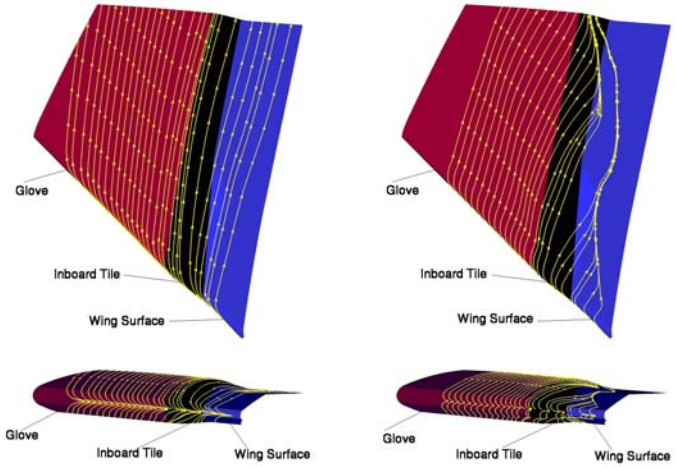

Figure 24. Streamlines (left) and friction lines (right) over the glove, tile and the inboard wing.

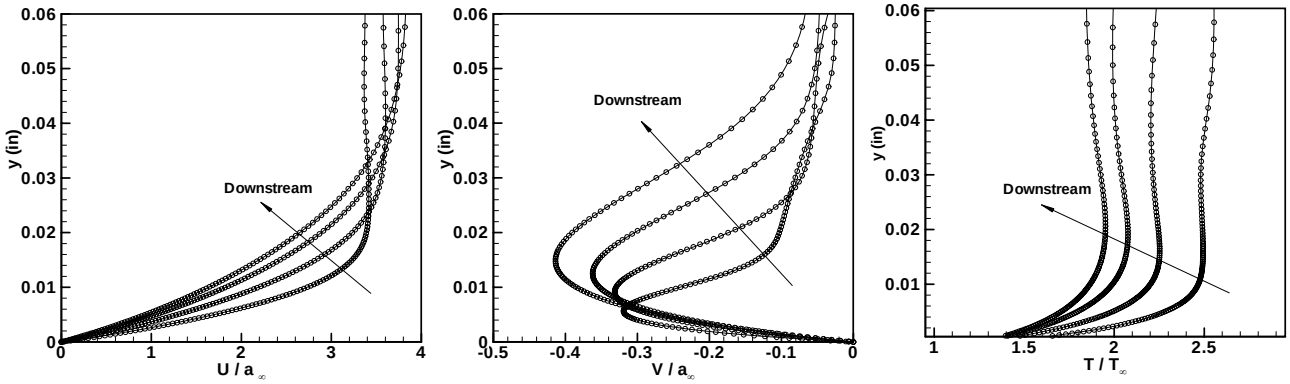

(a) streamwise velocity *(b) crossflow velocity* *(c) temperature*

Figure 25. Mean flow profiles at midspan of the glove at 1, 2, 3 and 4 inches from the leading edge, t = 50 sec.

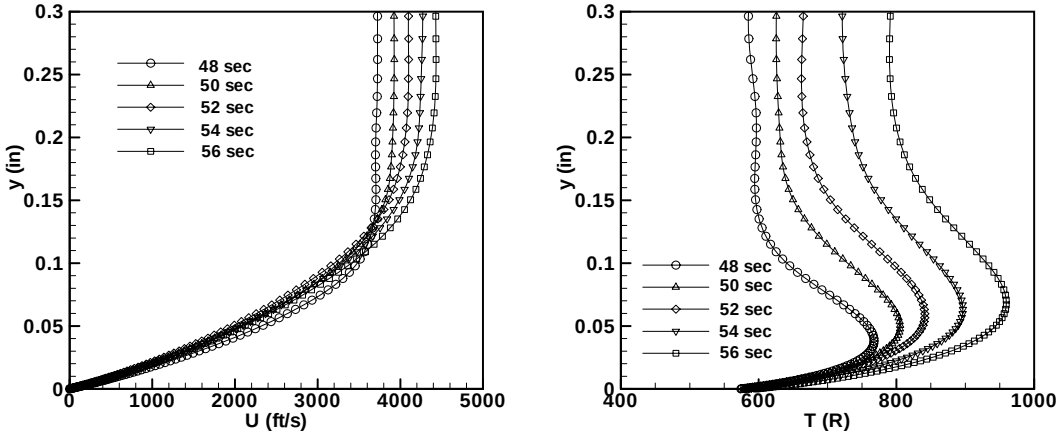

Figure 26. Streamwise velocity (left) and temperature (right) profiles at a point near the center of the glove for t = 48, 50, 52, 54 and 56 seconds, for G1 grid.

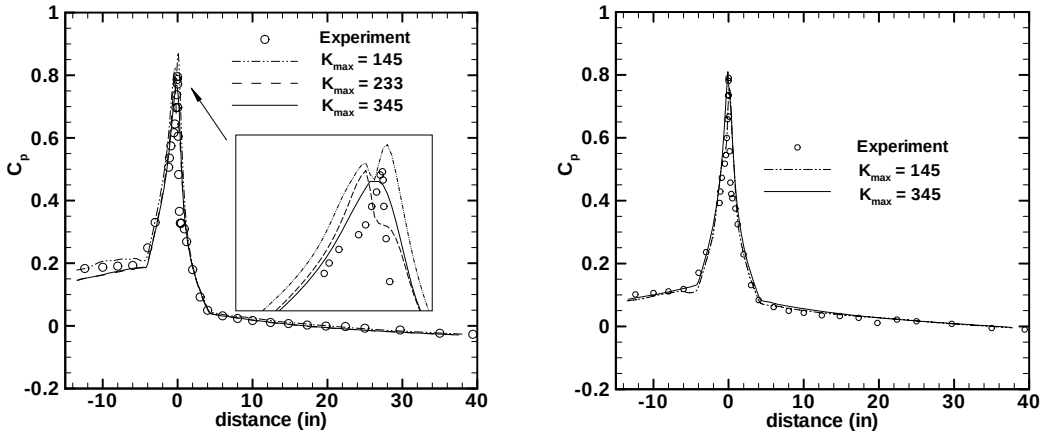

Figure 27. Cp distributions along the outboard row of pressure taps at t =50 sec. (left) and t= 56 sec. (right). The distance is measured from the leading edge of the wing along the row of pressure taps.

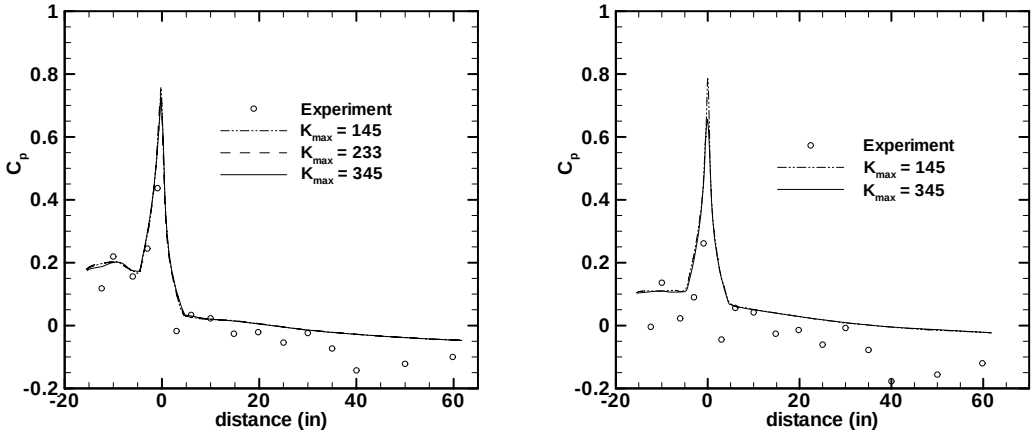

Figure 28. Cp distributions along the inboard row of pressure taps at t = 50 sec. (left) and t = 56 sec. (right).

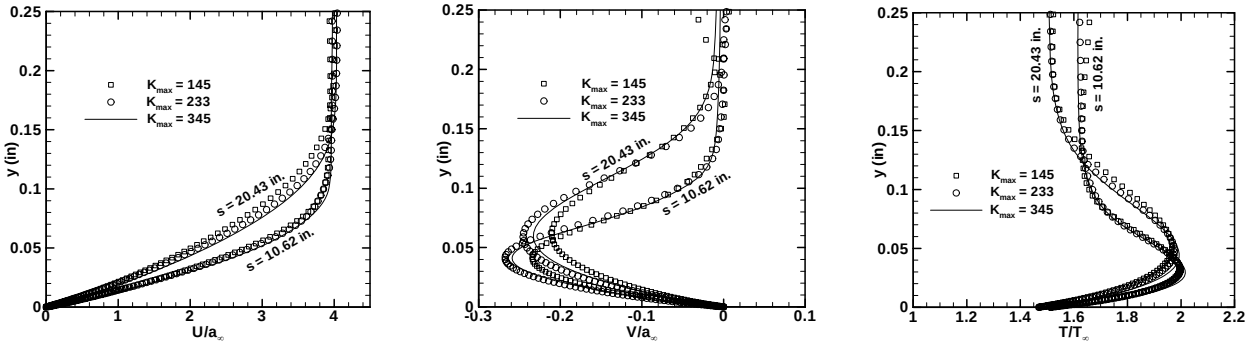

(a) streamwise velocity *(b) crossflow velocity* *(c) temperature*

Figure 29. Effect of grid on mean flow profiles at mid-section of the glove for t = 50 sec.

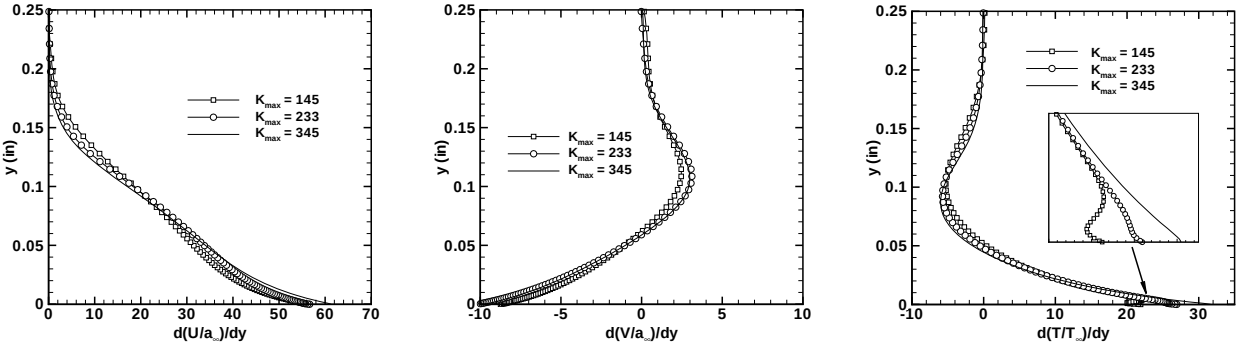

(a) streamwise velocity *(b) crossflow velocity* *(c) temperature*

Figure 30. Wall-normal derivative of mean flow profiles at the mid-section of the glove at 20.43 inches from the leading edge for t = 50 sec.

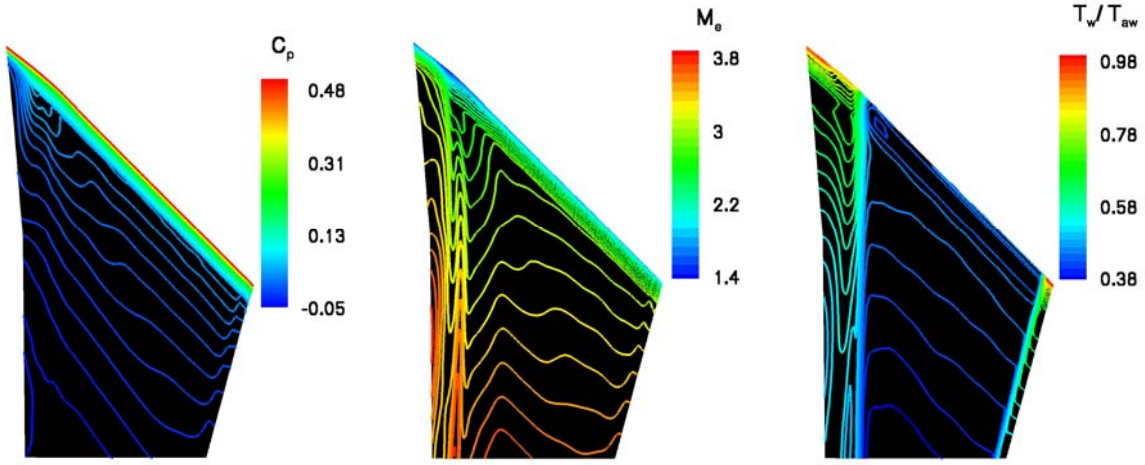

(a) pressure coefficient *(b) Mach number* *(c) temperature ratio*

Figure 31. Surface distribution of (a) pressure coefficient, (b) boundary layer edge Mach number and (c) ratio of wall temperature to adiabatic temperature.

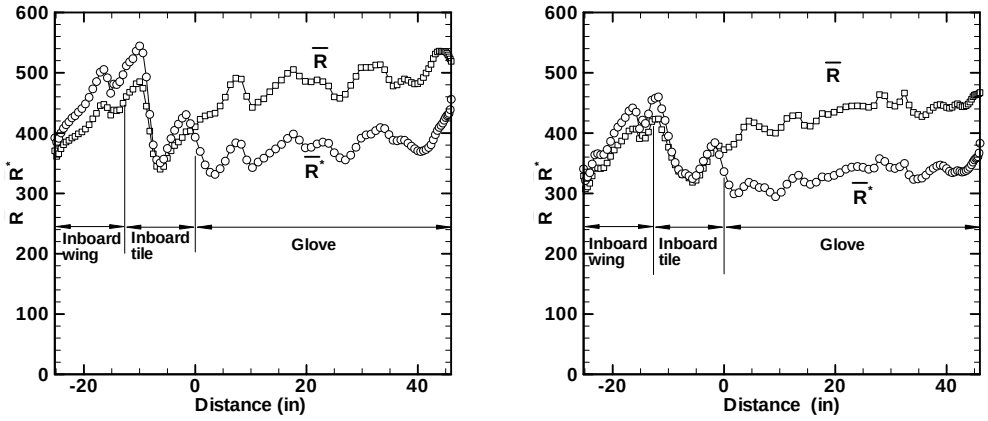

(a) t = 48 sec. *(b) t = 50 sec.*

Figure 32. Distributions of $\overline{R}$ and $\overline{R}^*$ along attachment line.

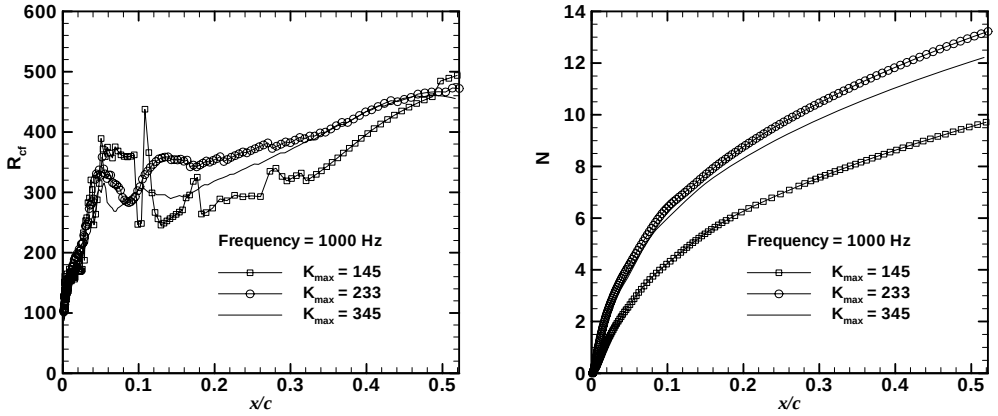

(a) Crossflow Reynolds number *(b) N-factor*

Figure 33. Effect of CFD grid on Crossflow Reynolds number and N-factors; results are along group velocity lines in the mid-span region of the glove.

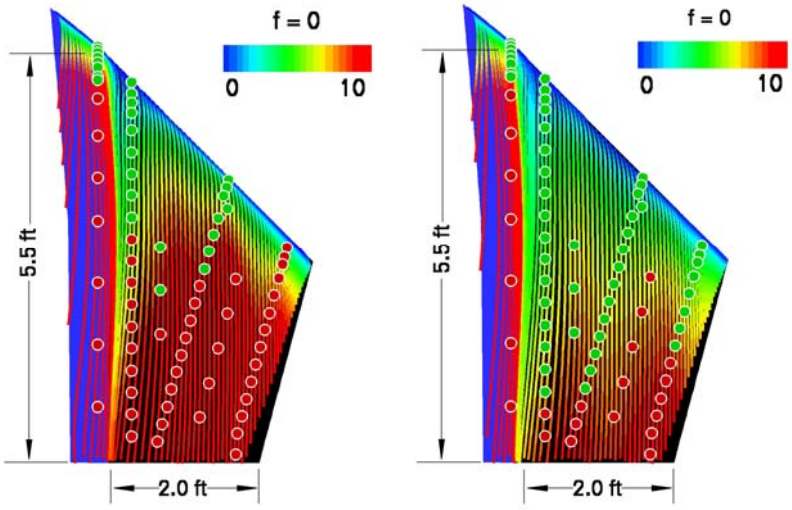

(a) t = 48 sec. *(b) t = 50 sec.*

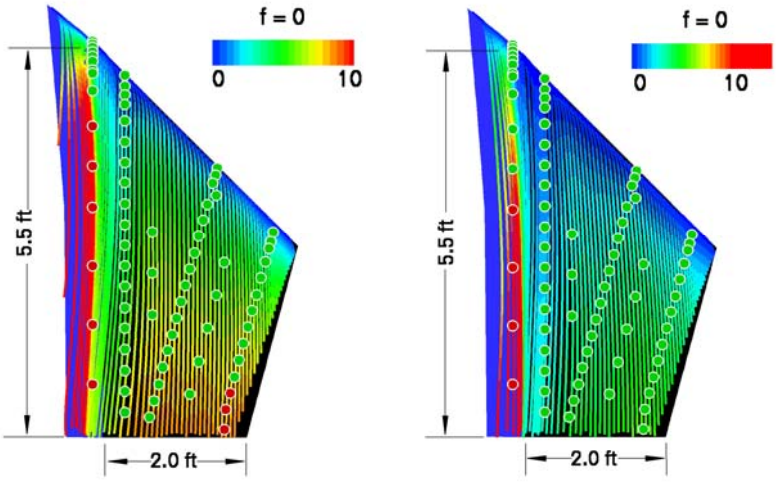

(c) t = 52 sec. *(d) t = 56 sec.*

Figure 34. N-factor traces for stationary crossflow disturbances. Thermocouple locations are indicated by green (laminar) and red (turbulent) dots.

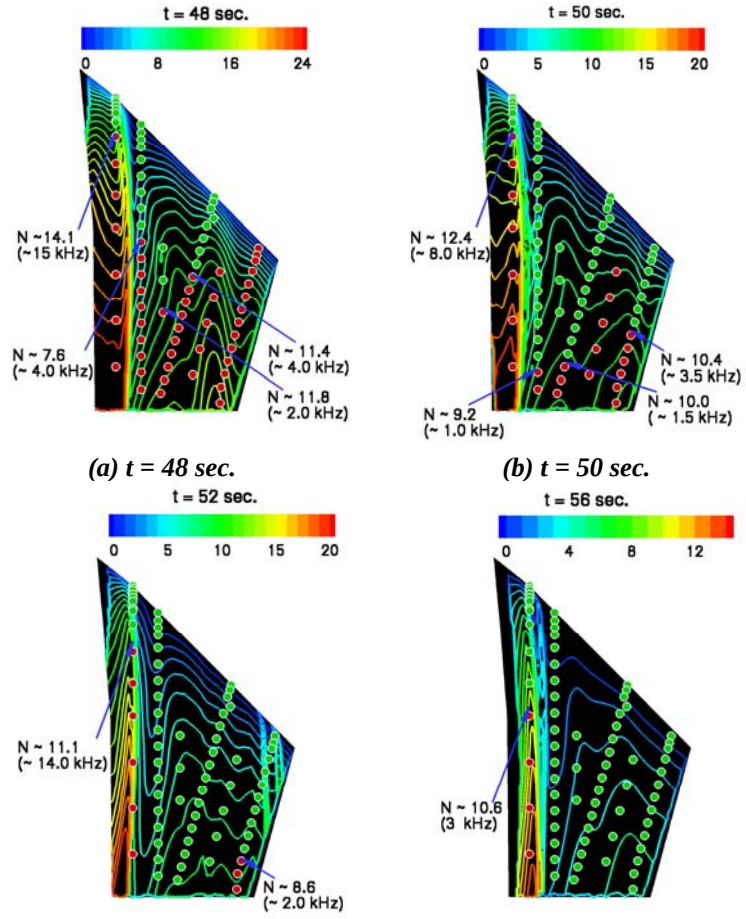

(a) t = 48 sec. *(b) t = 50 sec.*

(c) t = 52 sec. *(d) t = 56 sec.*

Figure 35. Contours of maximum N-factors (contour levels differ by 1). N-factor values at transition and the corresponding frequencies are indicated with blue arrows.

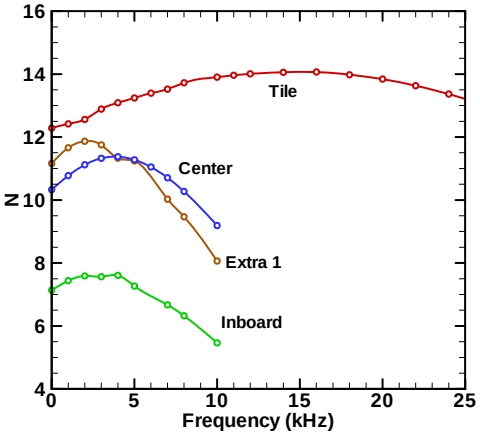

(a) t = 48 sec.

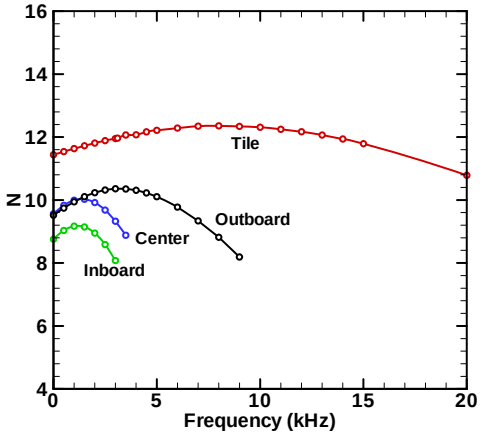

(b) t = 50 sec.

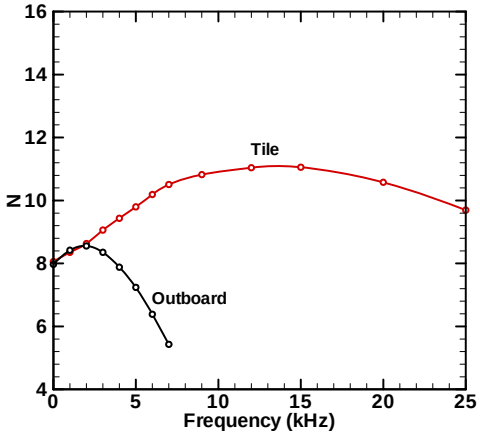

(c) t = 52 sec.

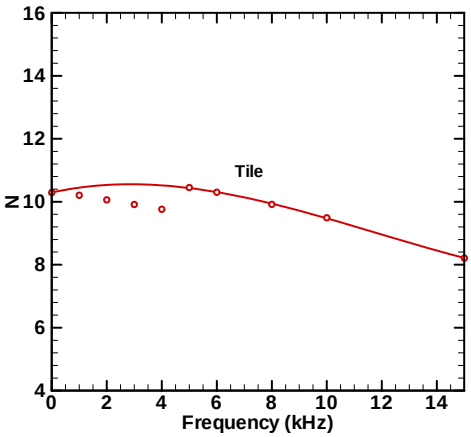

(d) t = 56 sec.

Figure 36. Frequency dependence of N-factors at transition locations along thermocouple rows over the glove and tile regions

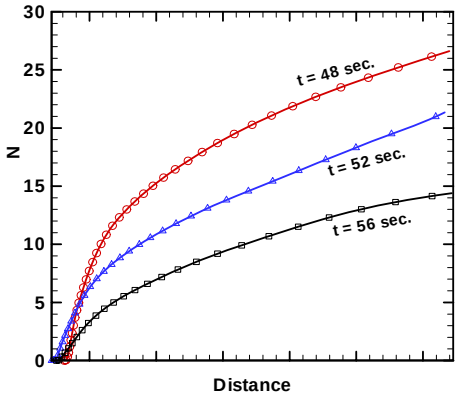

Figure 37. Tile region N-factor variation for stationary disturbances. Extrapolation to t = 60 sec. would indicate entire tile region to be laminar, consistent with experiment.

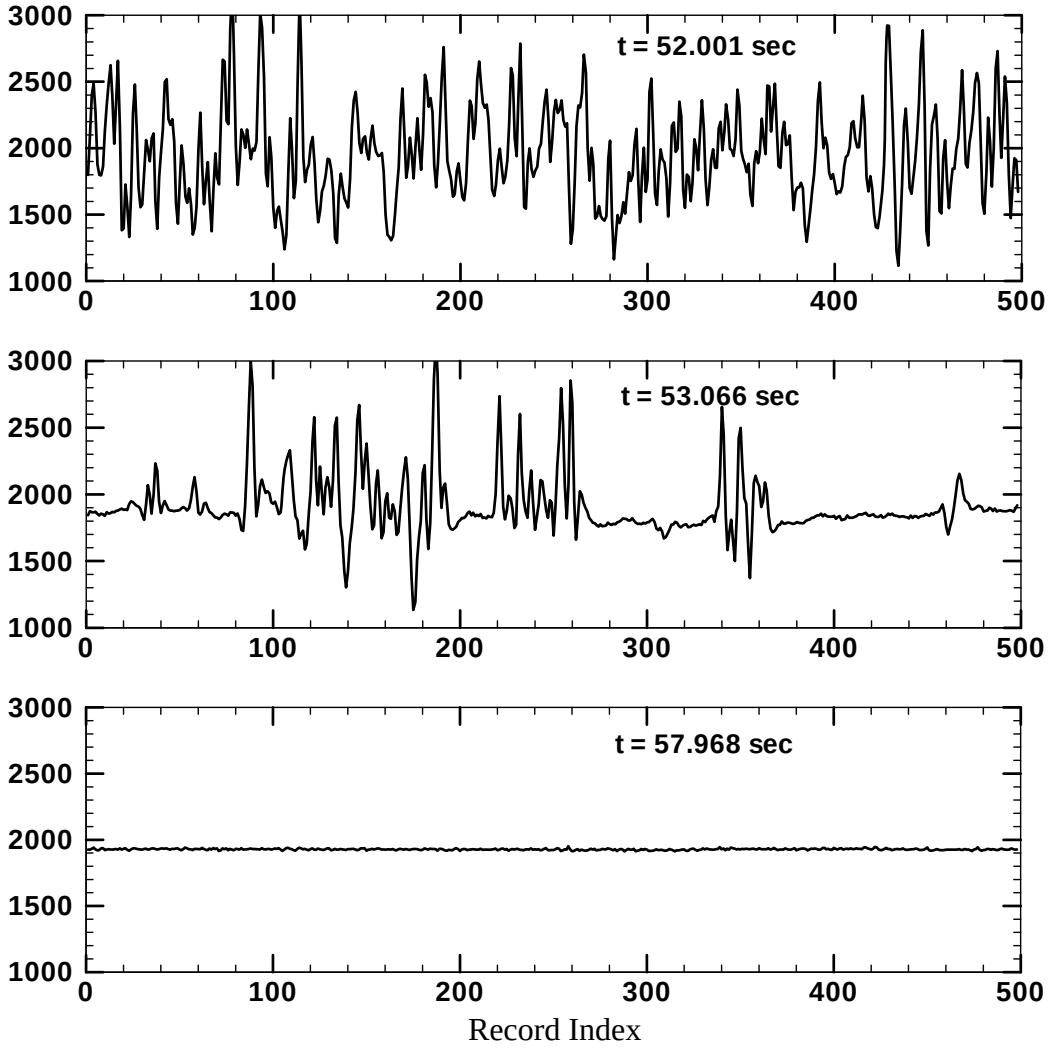

Figure 38. Channel 5 hot film signals; the indicated times correspond to the mid point of each record.

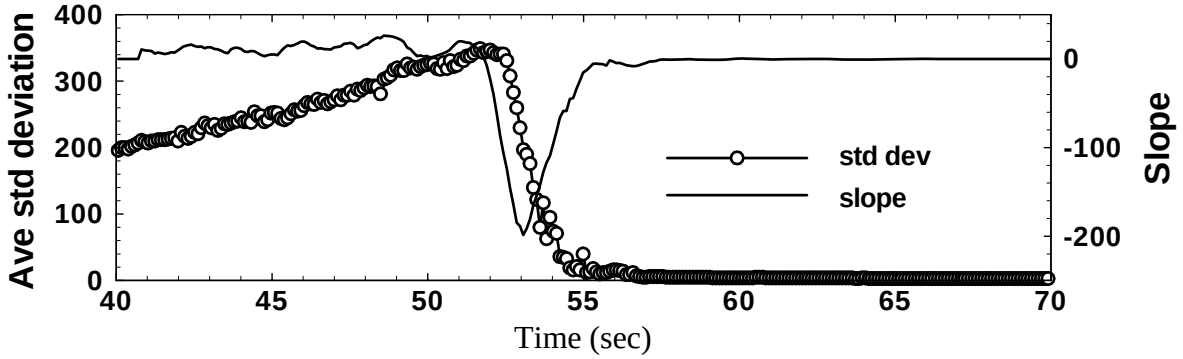

Figure 39. Averaged standard deviation curve and its slope for Channel 5 hot film signals.

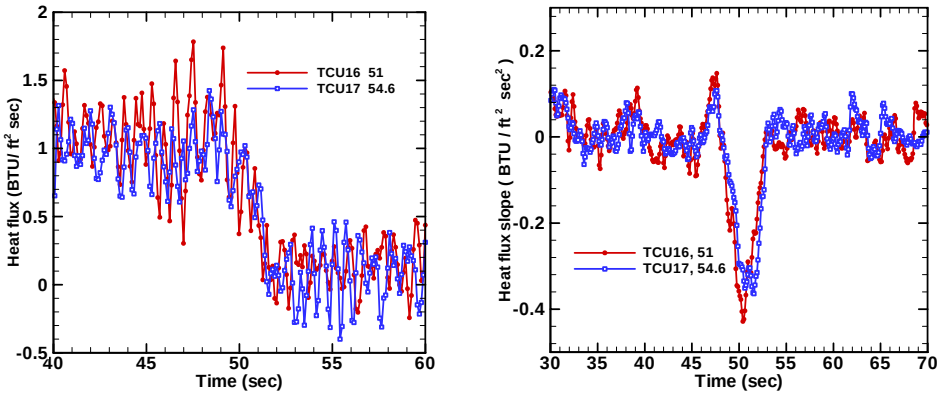

(a) Heat flux *(b) Heat flux slope*

Figure 40. Heat flux history and it slope for two thermocouples near Channel 5 hot film.

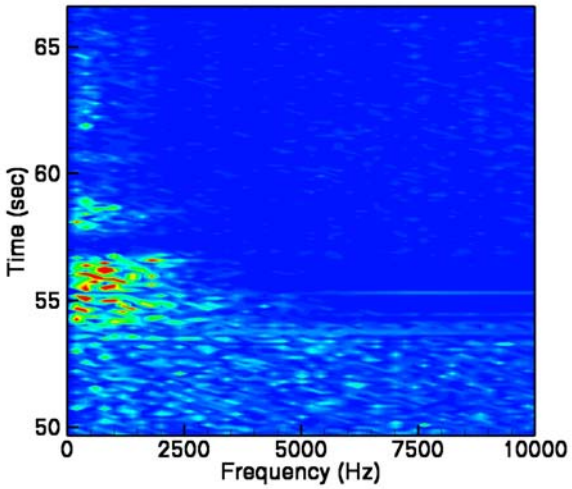

Figure 41 Power spectral density of channel 5 hot film signals.

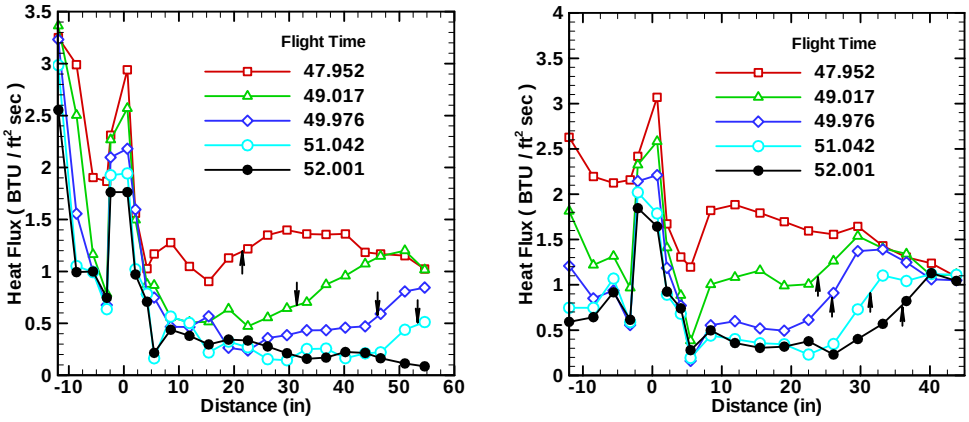

(a) Center row *(b) Outboard row*

Figure 42. Heat flux along center and outboard rows of thermocouples. Short arrows point to transition location from the "knee" approach.